



UNIwersytet  
Warszawski



---

Year: 2025

---

## **Studies on the Thermal Decomposition Mechanism at Diamond-Silica Interfaces Induced by Localized Laser Vitrification: experimental and ab-initio approach**

Robert Bogdanowicz; Krzysztof Pyrchla; Mateusz Ficek; Maciej J. Głowacki; Franciszek Skiba; Jacek Ryl; Justyna Gumieniak; Tatarczak, Piotr; Mirosław Sawczak; Marta Przeźniak-Welenc; Pascal Hänzi; Alexander Heidt; Wyszomłek, Andrzej; Buczyński, Ryszard; Klimczak, Mariusz

DOI: <https://doi.org/10.58132/HUQ9UU>

Posted at The Institutional Repository of the University of Warsaw  
ReIn UW: <https://repozytorium.uw.edu.pl/handle/item/166382>  
Unique UUID of the publication: 11dc616b-b390-40f6-910a-60dcf2b5d63a



The following work is licensed under a CC-BY - Attribution License.

# Studies on the Thermal Decomposition Mechanism at Diamond-Silica Interfaces Induced by Localized Laser Vitrification: experimental and *ab-initio* approach

Robert Bogdanowicz<sup>1\*</sup>, Krzysztof Pyrchla<sup>1</sup>, Mateusz Ficek<sup>1</sup>, Maciej J. Głowacki<sup>1</sup>, Franciszek Skiba<sup>1</sup>, Jacek Ryl<sup>2</sup>, Justyna Gumieniak<sup>3</sup>, Piotr Tatarczak<sup>4</sup>, Mirosław Sawczak<sup>5</sup>, Marta Prześniak-Welenc<sup>2</sup>, Pascal Hänzi<sup>6</sup>, Alexander Heidt<sup>6</sup>, Andrzej Wysmołek<sup>4</sup>, Ryszard Buczyński<sup>4,7</sup> and Mariusz Klimczak<sup>4\*</sup>

<sup>1</sup> *Gdańsk University of Technology, Faculty of Electronics, Telecommunications and Informatics, Narutowicza 11/12, 80-233, Gdańsk, Poland*

<sup>2</sup> *Faculty of Applied Physics and Mathematics, Institute of Nanotechnology and Materials Engineering, Gdansk University of Technology, Narutowicza 11/12, Gdansk 80-233, Poland*

<sup>3</sup> *Faculty of Mechanics and Technology Rzeszów University of Technology, Kwiatkowskiego 4 37-450 Stalowa Wola, Poland*

<sup>4</sup> *Faculty of Physics, University of Warsaw, Pasteura 5, Warsaw, 02-093, Poland*

<sup>5</sup> *Polish Academy of Sciences, The Szewalski Institute of Fluid-Flow Machinery, The Centre for Plasma and Laser Engineering, Fiszerza 14, 80-231 Gdańsk, Poland*

<sup>6</sup> *University of Bern, Institute of Applied Physics, Sidlerstrasse 5, 3012, Bern, Switzerland*

<sup>7</sup> *Łukasiewicz Research Network, Institute of Microelectronics and Photonics, Al. Lotników 32/46, 02-668, Warsaw, Poland*

\*email: rbogdan@eti.pg.edu.pl (R. Bogdanowicz) and mariusz.klimczak@fuw.edu.pl (M. Klimczak)

**Abstract.** This study investigates the thermal decomposition mechanisms at silica-diamond interfaces following localized laser vitrification, combining experimental analysis with molecular dynamics simulations. Two types of diamond particles were analyzed: NV-rich nanodiamonds (180 nm) and monocrystalline synthetic diamonds (154 nm). The samples were fabricated using vacuum-based CO<sub>2</sub> laser vitrification at a wavelength of 10.6 μm, designed to

overcome the processing temperature mismatch between diamond and silica. Scanning electron microscopy revealed distinct interface regions with localized defects measuring up to 10  $\mu\text{m}$  in diameter in monocrystalline diamond samples. Raman spectroscopy and fluorescence analysis demonstrated different decomposition for each diamond type, with NV-rich nanodiamonds exhibiting characteristic NV center emission at 637 nm. Thermogravimetric analysis coupled with mass spectrometry identified a multi-step decomposition process, with  $\text{CO}_2$  release occurring above 300°C and distinct thermal degradation temperatures depending on the diamond type. Molecular dynamics simulations using the Reax Force Field method elucidated the interface dynamics, revealing that amorphous silica accelerates  $\text{CO}_2$  release from carboxyl-functionalized diamond surfaces. These findings provide key insights into thermal decomposition at silica-diamond interfaces, contributing to the development of hybrid materials for quantum optics, particularly in low-loss magnetically sensitive optical fibers used in optomagnetometry.

**Keywords:** *nanodiamond particles, silica, laser-induced vitrification, molecular dynamics, thermal decomposition*

# 1. Introduction

Diamonds are renowned for their high thermal conductivity, with values reported up to 2000 W/mK for single crystal diamond, rivalling that of bulk diamond<sup>1,2</sup>. Nanodiamonds (ND) have lower thermal conductivity compared to bulk diamond due to size limitations and phonon propagation mechanisms<sup>3,4</sup>. Both ND and microdiamonds demonstrate remarkable thermal stability. ND, for instance, can resist transformation and maintain their phase stability up to temperatures around 800°C in an oxygen-free environment<sup>5-7</sup>. Microdiamonds have been shown to retain their crystalline structure even at elevated temperatures approaching 1400°C, provided that they are under suitable high-pressure conditions (2 - 8 GPa)<sup>8,9</sup>. The thermodynamic stability of nanodiamonds is of paramount importance during their incorporation into silicate matrices. Research by Qiao et al. demonstrated that nanodiamonds transition to graphitic, onion-like carbon structures upon annealing at 1400°C for one hour in an atmospheric environment<sup>10</sup>. Additionally, it has been elucidated that the thermal decomposition of oxygen-containing functional groups on nanodiamond surfaces occurs between 300°C and 900°C, while hydrocarbon (CH<sub>x</sub>) moieties decompose within a temperature range of 700°C to 1150°C<sup>11</sup>.

Diamond particles at the micrometer scale exhibit an increased resistance to graphitization within the thermal domain of 700-1400°C under the influence of pressures ranging from 2 to 8 GPa<sup>12</sup>. Under these conditions, nanodiamonds are less prone to transform into graphite, with a tendency to form microcrystalline graphite structures rather than onion-like carbons.

Butenko et al.<sup>13</sup> identified two predominant graphitization mechanisms that are active over distinct temperature regimes. The Debye temperature of nanodiamond, established at 1577°C, demarcates the boundary between these thermal spectra: (I) the penetration of external factors from the surface to the inner bulk of the diamond particle and (II) the detachment of surface groups that contribute to the stabilization of the crystal lattice periphery. Consequently, the thermal conductance properties of nanodiamond serve as a critical metric for determining the equilibrium between diamond and graphite phases<sup>14</sup>.

The integration of nanodiamonds into silica glass is driven by two key applications: magnetically sensitive optical fibers and fibers with engineered optical nonlinearity. Embedding NV-rich nanodiamonds in fibers enables distributed magnetic field sensing with high spatial resolution<sup>15</sup>. While this has been demonstrated in soft-glass fibers, extending it to silica-based fibers, widely used in optical networks, requires overcoming nanodiamond

degradation at high processing temperatures. Additionally, nanodiamond doping provides a unique means to tune the nonlinear optical response of glass, allowing for enhanced, reduced, or even negative Kerr nonlinearity <sup>16</sup>. This capability is highly relevant for ultrafast and nonlinear fiber optics, where independent control of dispersion and nonlinearity could lead to novel applications. Realizing such composite optical fibers remains challenging due to the thermal incompatibility of diamond and silica, particularly the risk of nanodiamond graphitization during vitrification. On the other hand, the composite glass should retain thermal stability, optical transparency, and preserve the nanodiamonds' functionalities. Ideally, the nanodiamonds should resist graphitization during high-temperature processing, ensuring their structural and optical integrity. Importantly, optical losses should remain minimal to support both groups of applications.

Phenomena occurring at the diamond and silica interface have been extensively studied using computer simulations based on the molecular dynamics and density functional theory <sup>17-19</sup>. From the experimental side and depending on the physical conditions, they can be differentiated into effects observable at low temperatures (i.e. without external application of high processing temperature) or at the diamond or silica processing temperatures. They can also be divided depending on the interacting Si material, i.e. silica or silicon, or the type of reaction atmosphere, i.e. oxidizing or non-oxidizing.

Instability of silica and diamond interfaces was manifested already at room temperature, for example in the form of increased diamond tool wear over silica surfaces, compared to other materials, including silicon <sup>19</sup>. This effect has been linked to the preservation of aromatic structures of the C-C atom bonds at the diamond crystal lattice termination and the depopulation of orbitals of those bonds in the presence of either an oxygen or a silicon atom during friction between the diamond and silica surfaces. This aromaticity preservation-driven activation of C-C bonds in diamonds enables their breaking and degradation of the diamond itself. Notably, it is a chemical activation process, and it does not depend on temperature. These findings should not indicate that the temperature activation processes are negligible in diamond-silica systems. On the contrary, molecular dynamics simulations suggest that thermal conductance of a diamond-silicon interface rapidly increases above the Debye temperature of silicon and even when the interface feature size remains below the phonon mean free path <sup>17</sup>.

It should be noted here that despite these challenges involving both the sensitivity of diamond to high-temperature processing and its atomic incompatibility in the context of forming stable interfaces with other materials, its successful integration with silica is feasible. In particular,

carboxylation of nanodiamonds has been demonstrated (and described theoretically using computer modelling) as means to suppressing the diamond electronic structure and enabling the growth of ultra-thin (up to 35 nm) layers of SiO<sub>2</sub> on diamond cores<sup>20</sup>. Processing of diamond at elevated temperatures in oxidizing or silicon-rich environments has revealed different behaviour depending on the diamond surface termination. For example, it has been shown that oxidation of initially hydrogenated diamond required desorption of the hydrogen, upon which the diamond surface covered with a graphitic layer<sup>21</sup>. This study also evidenced un-hydrogenated rough diamond surfaces with dangling bonds as significantly more susceptible to oxidation than the hydrogenated (100) surfaces of diamond. Notably, high graphitization resistance of the (100) diamond surface up to a temperature of 1700 deg. C has also been reported<sup>22</sup>. In the same work the conditions and parameters of silicon carbide formation through sintering of graphite-covered diamond overlaid with a silicon melt have been highlighted at the silicon melting temperature of 1390.8 °C. Although the crystallographic planes of diamond revealed different thermal stability (owing to the particular atom densities at the surface) and graphitization rates, the rate of silicon carbide impregnation occurring in the direction from the diamond-Si interface into the diamond crystal was significant, reaching the order of single cm/s. The degradation of diamond thermal stability can be suppressed in a non-oxide environment where directly bonded diamond and silicon surfaces showed interfacial stress relaxation even at a temperature 1000°C, owing to the formation of around 25 nm-thick layer of SiC<sup>23</sup>. Chemical vapor deposition (CVD)-grown diamonds doped with silicon have been shown to decrease the rate of surface oxidation by over 50% compared to undoped CVD diamond reference. This has been observed experimentally, following initial modelling using density functional theory-based computer simulations<sup>24</sup>.

Silica-diamond interfaces have emerged as a critical frontier in photonics and quantum sensing applications, yet the thermal decomposition mechanisms during laser vitrification of these composites remain unexplored. This study presents the first comprehensive investigation of thermal behavior at silica-diamond interfaces during localized laser processing, combining advanced experimental characterization with molecular dynamics simulations. We systematically examined two previously unexplored diamond species in this context: NV-rich nanodiamonds (NDNV, 180 nm) and monocrystalline synthetic diamonds (MSY, 154 nm), employing a novel vacuum-based CO<sub>2</sub> laser vitrification process at 10.6 μm wavelength to overcome the fundamental processing temperature incompatibility between diamond and silica matrices. Our multi-technique characterization approach revealed previously undocumented

interface phenomena. Scanning electron microscopy identified distinct compositional regions with precisely characterized defect distributions, while advanced spectroscopic analysis demonstrated differentiated decomposition pathways between NDNV and MSY particles, with NDNV samples exhibiting characteristic NV color center emission at 637 nm. Through coupled thermogravimetric-mass spectrometry, we identified multi-step decomposition mechanism, characterized by initial CO<sub>2</sub> release above 300°. Molecular dynamics simulations using the Reax Force Field method provided insight into interface dynamics, revealing catalytic effect of amorphous silica on CO<sub>2</sub> release from carboxylated diamond surfaces. These findings allow for understanding of thermal decomposition at silica-diamond interfaces, enabling the development of next-generation hybrid materials for quantum sensing and low-loss magnetically sensitive optical fiber applications.

## 2. Experimental

### 2.1. Diamond-in-silica glass sample fabrication

Silica-diamond samples were carefully fabricated and subjected to localized laser vitrification using state-of-the-art equipment. Two brands of nanodiamond particles were used in this study: *NDNV140nmHi* (aqueous suspension, 1 mg/mL) purchased from Adámas Nanotechnologies (USA), and *MSY 0-0.25 micron* acquired from Pureon AG (Switzerland). Both kinds of the particles were produced using the high-pressure high-temperature (HPHT) process and show similar size distributions (Fig. S1). The key difference is that *NDNV140nmHi* are implanted with NV color centers and carboxyl-terminated. For the vitrification process, both brands of the nanodiamonds were suspended in ethyl alcohol (99.8%, pure p.a.), which was supplied by Chempur (Poland).

The *NDNV140nmHi* aqueous suspension was homogenized in the Sonic-3 ultrasonic bath (Polsonic, Poland) for 30 min at room temperature. Afterwards, small volume (4 mL) of the suspension was placed in the DZ-2BCII vacuum drying oven (Chemland, Poland) and dried at 60°C under low vacuum (pressure of -0.1 MPa) for 5 days. The dried residue was redispersed in ethanol to produce the suspension with 1 mg/mL concentration of diamond. The redispersion process was performed using the Bandelin Sonopuls HD 4200 ultrasonic homogenizer (Bandelin electronic GmbH & Co., Germany) equipped with the TS106 probe. The homogenizer was set to pulsed mode (0.5-s working step per 0.5-s idle step) at 40% amplitude. The total time of the sonication was 50 min. Dynamic light scattering (DLS) was used to

confirm proper redispersion of the particles (Fig. S1). The *MSY 0-0.25 micron* particles were directly dispersed in ethanol to produce the suspension with 1 mg/mL concentration of diamond. The dispersion process was facilitated by 45-min sonication in the ultrasonic bath. Again, the successful dispersion was verified using DLS (Fig. S1).

The DLS measurements were carried out on the Zetasizer Nano ZS particle analyzer (Malvern Panalytical, UK). equipped with the 4-mW He-Ne laser ( $\lambda = 632.8$  nm) and the narrowband filter (ZEN9062). The samples were placed in disposable, macro-volume polystyrene cuvettes ( $12 \times 12 \times 45$  mm outer dimensions) and examined at 25°C in a backscatter configuration (scattering collected at 173° angle). Average hydrodynamic diameters ( $Z_{Ave}$ ) were derived from the cumulants analysis (Fig.S1) performed using the following properties of ethanol: dynamic viscosity of 1.074 cP, refractive index of 1.361 . Volume-weighted particle size distributions (Fig. S1) were calculated using the following characteristics of nanodiamonds: refractive index of 2.42, extinction coefficient of 0.0<sup>25</sup>. To prepare the samples for thermogravimetric analysis, water-based nanodiamond suspensions with very low concentrations were produced. The aqueous *NDNV140nmHi* suspension (1 mg/mL) was diluted with deionized water to obtain 0.1 mg/mL suspension. The sample was vortexed at 2 500 RPM for 5 min using the TX4 digital vortex mixer (VELP Scientifica, Italy). The *MSY 0-0.25 micron* particles were dispersed in deionized water in 0.05 mg/mL concentration and treated in the ultrasonic bath for 45 min. Deionized water was produced using the HLP Smart water purification system (Hydrolab, Poland). The suspensions were added to 1-gram portions of SiO<sub>2</sub> powder suspended in 2.5 mL of isopropyl alcohol in a range of ratios (Table S1). Every sample was magnetically stirred at 500 RPM for 30 min, and then dried overnight in the oven (without vacuum) at 60°C. Dried mixtures were analyzed using TGA/DSC coupled with mass spectrometry.

**Table 1** - Parameters of Diamond-in-Silica glass samples.

Sample label	Nanodiamond type	Concentration (mg ND/ g silica)	Vitrified perform optical quality
NDNV-SIO2	180 nm, NV—nanodiamond	0.01	Suitable for fiber drawing, optical quality
MSY-SIO2	154 nm, MSY particles	0.01	Suitable for fiber drawing, optical quality

The preparation of diamond-doped silica glass samples presents significant challenges due to the inherent incompatibility between diamond and silica processing temperatures. This is particularly evident in the limited literature addressing bulk incorporation of nanodiamonds into

silica glass preforms. Our investigation focuses on two distinct sample series: NDNV-SiO<sub>2</sub>, comprising NV-rich nanodiamonds (180 nm primary fraction) previously investigated for physicochemical interface properties (Ref. <sup>16</sup>), and MSY-SiO<sub>2</sub>, featuring monocrystalline synthetic diamond particles (MSY, 154 nm) not previously studied in silica glass matrices (Table 1 contains full sample lineup). This comparative approach enables systematic evaluation of diamond-silica interface formation and its influence on optical properties across different diamond particle types.

In each case of all glass sample series studied here, the initial mixture was homogenized, after which the ethanol was evaporated. For the vitrification procedure itself, schematically illustrated in Fig. 1, the diamond-silica blend was placed in a silica tube 4 mm in diameter, 1 mm wall thickness, 20 cm long, and dried overnight at 300°C in a vacuum. This pre-heating temperature was selected such that the residual moisture and organic contaminants would be removed, while this process was still carried out well below the temperature of 600°C in which significant weight loss is observed in diamond. After this, the mixture inside the tube was vitrified to optical quality glass rods by scanning the tube with a light blade from a continuous-wave, high-power, CO<sub>2</sub> laser (Bystronic, Switzerland, wavelength of 10.6 μm).

Laser vitrification was performed using a custom-built, computer-controlled vitrification lathe that rotates and translates the silica tube vertically through the laser beam (~9 mm high, ~20 mm wide, 1/e<sup>2</sup> values). Key parameters such as laser power, rotational and translational speed are precisely controlled, with optional vacuum application. The setup allows for preform lengths up to 23 cm (see <sup>26</sup> for more technical details).

Laser vitrification is a key factor for successfully integrating nanodiamond into silica despite their significantly different processing temperatures. The process enables precise thermal control through the formation of an ultra-thin heat blade (~4.5~mm high) and steep temperature gradients (~100°C/mm). As the preform is vertically translated through the laser beam, each section experiences only brief high-temperature exposure, minimizing prolonged thermal interactions that could degrade the nanodiamonds. The strong heat localization allows vitrification of silica at temperatures exceeding 1500°C while promoting rapid cooling, which helps preserve a significant fraction of the nanodiamonds and ensures high-quality glass formation.

The laser outpower and the feed rate (determining the laser scan rate) were the two process parameters that were adjusted by trial and error to achieve optical quality of the vitrified material. In addition to that, different nanodiamond concentrations were tested and for some combinations multiple tests were done to find the right laser power and tube feed (laser scan)

rate for optical-quality sample vitrification. The criteria established for selecting optimal processing parameters were (i) obtaining clear glass without bubbles or scattering centers, (ii) absence of agglomerates of non-vitrified material, and (iii) absence of visible defects such as cracks or voids.

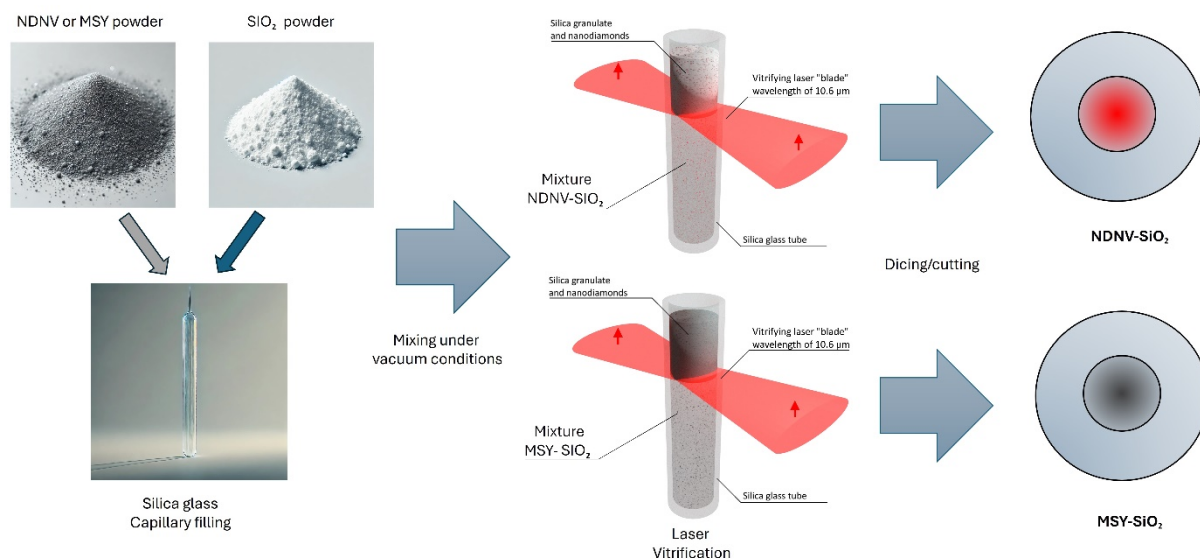


**Fig. 1.** Schematic of the diamond-silica samples fabrication involving laser blade-based vitrification.

The series labelled NDNV-SiO<sub>2</sub> contained 10 μg NV diamonds per 1 g of silica granulate. The optimized parameters in terms of the achieved optical quality were determined to be 200 W of laser power on the sample and 1.5 mm/min feeding speed, and other rods were produced using these settings. The vitrification was successfully repeated twice with the MSY diamonds. In the series labelled MSY-SiO<sub>2</sub> we used a concentration of 30 μg of MSY particles per 1 g of silica. The processing parameters used for this sample series were the parameters that yielded the best optical quality in the NDNV-SiO<sub>2</sub>.

## 2.2. Characterization Techniques of vitrified Diamond-in-Silica samples

### 2.2.1 Scanning Electron Microscopy (SEM)

SEM analysis was conducted to examine the surface morphology and microstructure of the vitrified samples. An FEI Quanta FEG 250 Scanning Electron Microscope (SEM) with a 10-kV beam accelerating voltage with a SE-ETD detector (secondary electron—Everhart—Thornley detector) in high vacuum mode (pressure 10<sup>-4</sup> Pa) was used to record the SEM images.

### 2.2.2 Raman Spectroscopy

Raman spectroscopy was employed to investigate the structural changes and chemical bonding at the interfaces. Raman measurements excited by 532 nm and 633 nm continuous-wave lasers were performed using a Horiba JobinYvon T6400 spectrometer, working in a single grating mode. An optical objective  $\times 100$  was used to achieve laser light spots below 1  $\mu\text{m}$  in diameter at the surface of the vitrified silica samples. To avoid sample degradation maximum laser excitation powers were about 5 mW and 2.5 mW, respectively. The same spectrometer but equipped with  $\times 40$  near-UV objective providing spatial resolution of about 1  $\mu\text{m}$  was used to collect Raman spectra with 325 nm continuous wave laser excitation source with a maximum power of about 3.5 mW. A Renishaw inVia Raman system equipped with a  $\times 100$  objective was used to record Raman spectra under 785 nm continuous wave laser excitation. In this case the maximum excitation power below 4.5 mW was used. No heating effects were observed.

### 2.2.3 Fluorescence Analysis

Fluorescence analysis provides insights into the optical properties and defect structures within the vitrified region. Fluorescence was excited at 532 nm with a Nd:YAG SHG cw laser (Millenia, Spectra Physics) emitting a beam of 500 mW. The laser beam was focused on a glass sample placed on a monocrystalline silicon substrate, which does not show a self-fluorescence signal when excited by a laser. Fluorescence from the sample was collected at an angle of 45 degrees to the laser beam. The optical signal was collected using a quartz lens and focused on the optical fiber of spectrometer. To block the laser radiation the bandpass filter (OG570, Schott) was used in the detection path. The fluorescence signal was analysed by means of a 0.3 m monochromator (SR303i, Andor) equipped with 600 groove/mm grating and recorded with an iCCD detector (DH740, Andor).

### 2.2.4 X-ray Photoelectron Spectroscopy (XPS)

High resolution XPS spectroscopy was carried out using Escalab 250Xi spectroscope (ThermoFisher Scientific), operating an AlK $\alpha$  X-ray source, with a spot diameter of 200  $\mu\text{m}$  and pass energy of 20 eV. The measurements were carried out in the sample breakthrough, done directly before the analysis to avoid surface contamination. Peak calibration was made using adventitious carbon C 1s (284.7 eV) and Si-OC Si 2p<sub>3/2</sub> for reference silica sample (103.0 eV). Spectral deconvolution was performed using Avantage v5.921 software provided by the spectroscope manufacturer.

### 2.2.5 Thermogravimetric Analysis

TGA coupled with Mass Spectrometry is used to study the thermal decomposition behavior and analyze decomposition products. In our study the thermogravimetric analysis (TGA) was performed under an argon atmosphere (flow rate 60 cm<sup>3</sup>/min) with a heating rate 10°C/min from 40°C to 1175°C using Netzsch STA 449 F1 Jupiter®. Constant sample mass (1000±5mg) was used. The thermal behavior has been also studied with mass spectrum (MS). The gases that come out from a sample during heating were monitored by the quadruple mass spectrometer Netzsch QMS 403C Aëolos. The mass spectra were measured from m/z 2 to 60. The measured peak intensities were analyzed as a function of the reaction time. If the difference between the background level and the highest intensity value was close to the noise level, the given mass spectrometric ion was rejected. To compare the intensity of the remaining m/z ion currents, the background of carrier gas was subtracted.

### 3. Computational Models For Simulations of Diamond-Silica Interfaces

Molecular dynamics (MD) simulations are conducted to investigate the dynamic behaviour of atoms and molecules at the interface under high-temperature conditions. The Reax Force Field method was used for the modelling of the system because of its effectiveness in the prediction of thermodynamic phenomena in both solid, gas and liquid phases<sup>27</sup>. It allows for studying the system of size and timescale inaccessible by quantum-mechanical calculations while still preserving the correct description of the process, such as phase transformation, defect formation and diffusion<sup>28</sup>. In contrast to AMBER<sup>29</sup>, CHARMM<sup>30</sup>, and other classical force fields, the process of bond breaking and formation is allowed and correctly described within this framework. These characteristic features make the REAX FF method an appropriate approach for the theoretical study of the thermal and chemical stability of diamond interfaces<sup>31,32</sup>.

For this work, two atomic models of the diamond-silica glass interface were created using the Quantum ATK software<sup>33</sup>. The first model represents the [111] diamond surface and the second [100] diamond surface. To replicate experimental conditions, both surfaces have been covered by a uniform, high-density carboxylic groups film. The theoretical maximal density of packing for carboxylic groups is approximately 50%<sup>34</sup> for a perfect diamond [100] or [111] surface. For higher coverages, the bond breaking and crosslinking process is unavoidable at any temperature. Under real conditions, because of surface imperfections and finite temperature effect, the achievable carboxyl coverage is much lower. Since the goal of this simulation experiment was to study the thermal disintegration of carboxyl functionalized diamond-silica

interface, the high concentration of these functional groups was desired. The stable configuration with the highest surface concentration, according to tests employing COHSi REAX force field <sup>32</sup>, performed for the pristine diamond surface model was 33%. For those reasons, 33% of reactive sites were carboxyl functionalised, and the rest were terminated with hydrogen to remove all dangling bonds. In the case of the [100] surface the carbon atoms were reconstructed according the 21 C(100) scheme as described in <sup>35</sup>. The atomic models of the interfaces are illustrated in Fig. 2.

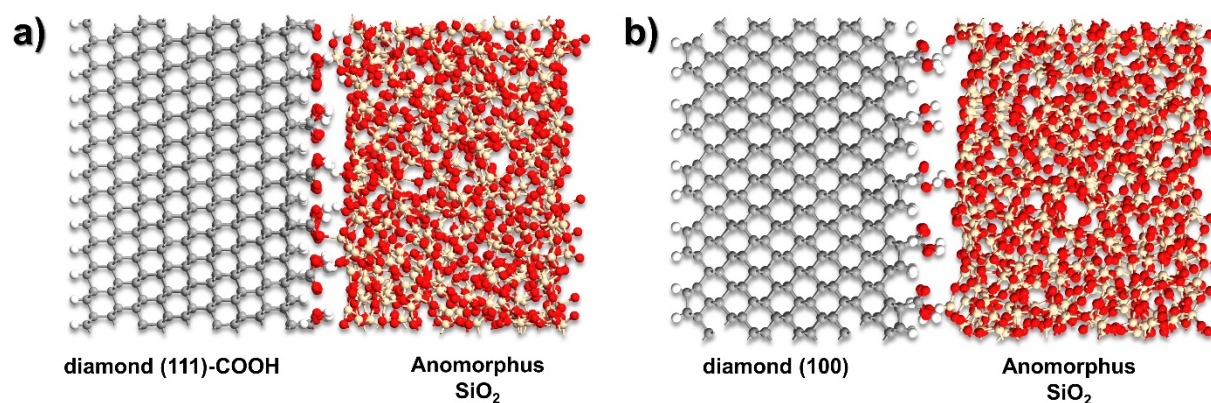


**Fig. 2.** Optimized model structures of diamond-silica interfaces: (a) COOH-terminated reconstructed diamond (111 12×12 unit cells) and amorphous silica emulating NDNV-SiO<sub>2</sub> interface; (b) COOH-terminated reconstructed diamond (100, 10×10 unit cells) and amorphous silica emulating NDNV-SiO<sub>2</sub> interface, the size was selected to keep the real space dimension of both slabs as close to each other as possible.

The surface model of amorphous silica was prepared separately, using the Quantum ATK software. As the starting configuration, the ideal cristobalite bulk crystal structure was used. This structure was melted in molecular dynamics simulation using NVT Langevin ensemble at temperature 5000 K. This initial step was undertaken to provide sufficient atomic position randomisation. The atomic interactions were described using the Pedone Fe2 2006 Force Field <sup>36</sup>. To achieve physical distribution of atoms, after first 200 ps of simulation at 5000 K the colling process was initialised. For next 500 ps the NPT Martyna Tobias Klein ensemble was set to the system and the reservoir temperature was lowered linearly from the 5000K to the 300 K. The resulting configuration was strained to fit the size of diamond surface and placed in 5 Angstroms from the surface. Then the atomic position were optimized using LBFGS method and subjected to the molecular dynamic simulation with NVT ensemble at temperature 300 K, for 300 ps which let the interface to form which was observed by the stabilisation of the distance between the diamond and silica surfaces. At this stage the description of the atomic interaction

was provided by the COHSi REAX force field with the parametrisation from Ref. <sup>31</sup>. The final form of the interfaces models is presented in Fig. 2. All numerical simulation, leading to the creation of the models were conducted using the LAMMPS software <sup>37</sup>.

## **4. Results and discussion**

### **4.1 Experimental Findings**

#### **4.1.1 Microstructural Insights Using SEM Analysis**

Figure 3 presents transmitted light microscope micrographs and SEM images of diamond-silica fabricated by the vitrification process. Both NDNV-SiO<sub>2</sub> and MSY-SiO<sub>2</sub> samples are of acceptable optical quality, and the transmission microscopic images shown in Fig. 3 reveal their transparency without observable macroscopic defects or precipitates as well as agglomerates. The central region of the sample contains the diamond-incorporated region while the outer region is the bare silica capillary, which was used to guide the vitrification process (shown in a diagram in Fig. 1). Samples are fully transformed from SiO<sub>2</sub> powder–diamond particle mixture into uniform and vitrified diamond-rich glassy composites.

To obtain the samples, a number of processes were carried out to optimize the diamond and silica blend but the key optimization parameter was to limit the laser power to minimize the temperature of the vitrification process so as to mitigate the thermal decomposition of the diamond. Qualitative information is provided by SEM images providing contrasting changes resulting from the interaction of electrons with samples. The top NDNV-SiO<sub>2</sub> sample in Fig. 3A.1 shows a highly homogeneous composite structure with few defects, which are clearly observed at the magnification on the right. Most of the sample area is homogeneously vitrified and the precipitates are due to locally defected vitrification disturbed locally by either agglomeration of smaller diamond particles or inclusion of larger grains because such can also exist in minimal amounts in the mixture. We note that the powder used was produced by ball-milling of a larger HPHT crystal. The number of defects is small and they have diameters in the range of single micrometers. Agreeably, these can introduce light scattering, but due to their minor quantity, this scattering is negligible. In the SEM images of the NVND-SiO<sub>2</sub> sample, it is difficult to observe differences between the central diamond-enriched area and the outer area, which is the pure silica capillary supporting the laser vitrification process.

The NDNV diamond used in the silica sample fabrication has undergone nitrogen implantation and electron irradiation and has been deeply treated in acids to etch defects and obtain high surface purity prior to the vitrification procedure <sup>38</sup>. These factors proved to be crucial for

suppressing, minimizing, and shifting the thermal decomposition threshold of the diamond grains to slightly higher temperatures, as confirmed by the TGA/DSC results and proven by obtaining homogeneous vitrification without a critical level of glass defect formation due to graphitized forms <sup>39</sup>. In both samples, similar limited laser powers were applied, and the concentrations of diamond grains were maintained at 0.01 mg per gram of silica.

The MSY-SiO<sub>2</sub> sample reveals a distinctly different topographic and structural character, being a bare ball-milled HPHT crystal with an undefined surface termination with a significantly higher amount of surface defects and contaminations <sup>40</sup>, as confirmed by the Raman studies presented in the next chapter. The complex of these diamond grains mixed with SiO<sub>2</sub> undergoes an intense chemophysical reaction induced by the elevated temperature from the laser source. The effect of a lower thermal decomposition threshold of the MSY grains is also visible in the TGA/DSC results. In the SEM images displayed in Fig. 3 B.1, the inhomogeneous central areas incorporated with diamond and the outer area of pure SiO<sub>2</sub> can be clearly distinguished. The defect concentration in this sample is high, with diameters up to around 10 μm and average spacings between defects in the range of 20-30 μm. The intense decomposition of diamond in this sample generated graphitized carbon forms disrupting the vitrification process creating improperly vitrified degenerated amorphous structures of SiO<sub>2</sub> heavily doped with carbon.

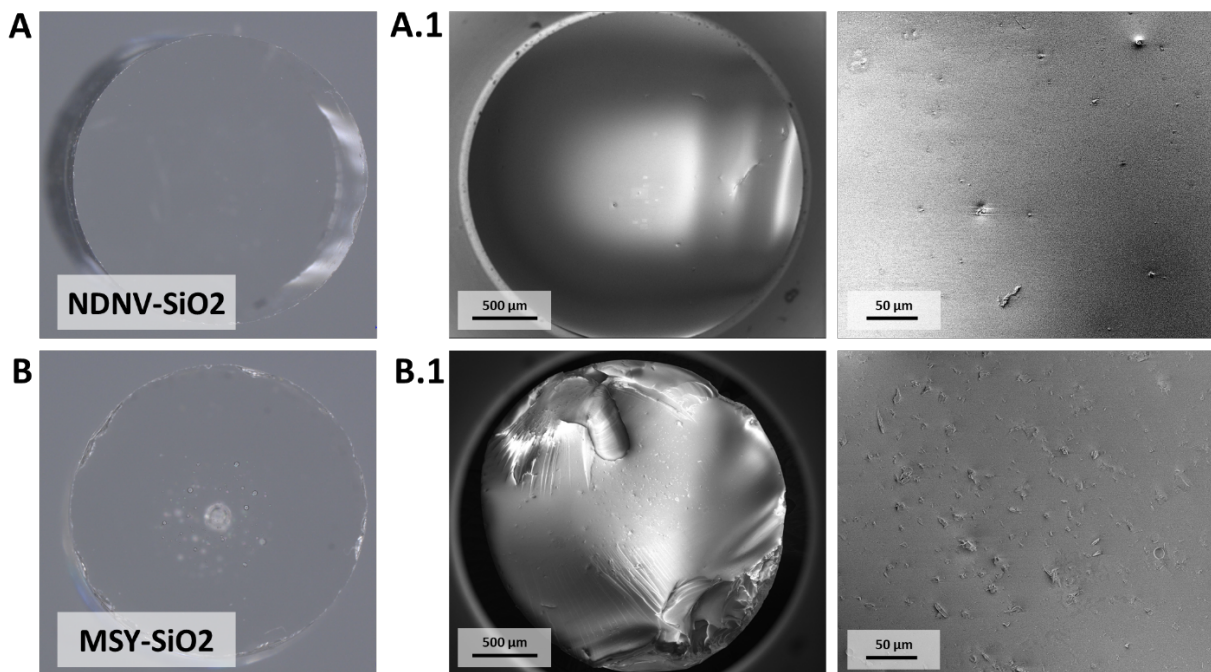


**Fig. 3.** Imaging of diamond-silica glass samples fabricated during the vitrification process: (A) NDNV-SiO<sub>2</sub> – transmitted light microscope micrographs, (A.1) SEM microimages followed

by magnified central region of the sample; (B) MSY-SiO<sub>2</sub> – transmitted light microscope micrographs, (B.1) SEM microimages followed by magnified central region of the sample.

Significant contrast differences were observed between the NDNV-SiO<sub>2</sub> and MSY-SiO<sub>2</sub> samples using back-scattered electron SEM imaging. The NDNV-SiO<sub>2</sub> sample exhibits a small number of brighter defects, indicating a minor level of graphitization, as shown in Fig. S2A. Image of MSY-SiO<sub>2</sub> presented in Fig. S2B shows a high density of black defects attributed to graphitized diamond particles.

The increasing of laser power during vitrification revealed more intense interactions between each type of diamond particles and SiO<sub>2</sub>, and the tendency that the NDNV was more stable than MSY was maintained. The process of thermal decomposition of diamond is further catalyzed by silica, which also undergoes decomposition, and the released oxygen reacts with carbon to form CO<sub>2</sub>, while the degenerated silica forms amorphous SiO. In the case of high-power application, macroscopic bubble-like holes appear in the place of diamond particle-rich areas, barely visible as defect shells in the MSY-SiO<sub>2</sub> sample as shown in magnified Fig. 3B.1. The holes have diameters of 100-500 μm, as seen in Fig. S3 in the supplementary information. The bubbles occur exclusively in the central area, which was enriched with diamonds. The formation of these bubbles results from the release of gases, mainly CO<sub>2</sub>, during the highly energetic vitrification process, further confirmed by the MD simulation results at a higher temperature shown as subsequent stages of interface decomposition at the bottom of Fig. S3 in the supplementary information. The thermal decomposition of diamonds and various species present on their surface leads to the generation of CO<sub>2</sub> and CO gas, as described by Butenko *et al.*<sup>11</sup>. Tailoring and optimization of vitrification conditions allowed us to achieve diamond-silica composite samples with indistinguishable central and outer areas.

#### **4.1.2 Spectroscopic Features induced by Thermal Decomposition – Fluorescence and Raman studies**

Raman spectra of the investigated NDNV nanodiamonds and MSY particles were collected under 532 and 785 nm laser excitation. Representative spectra are presented in Fig. S4 (supplementary information). In both cases, the center of the diamond-related Raman peak is close to the literature value of 1332 cm<sup>-1</sup><sup>41</sup>. However, the signal originating from MSY particles is broader, indicating that their structural quality is worse than that of NDNV nanodiamonds. In the next step, Raman mapping measurements of NDNV-SiO<sub>2</sub> and MSY-SiO<sub>2</sub> samples under

785 nm laser excitation with the step of 20  $\mu\text{m}$  have been performed. Fig. 4 a), b) show maps of total integrated intensity in the range 1200-1800  $\text{cm}^{-1}$ .

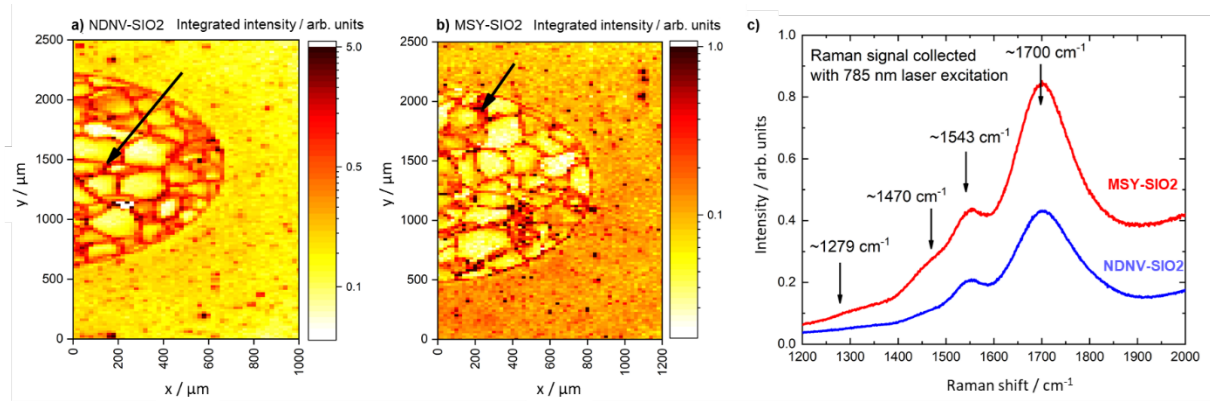


**Fig. 4.** Results of Raman mapping measurements under 785 nm laser excitation. a) and b) maps of total integrated intensities in the range 1200-1800  $\text{cm}^{-1}$  for NDNV-SiO<sub>2</sub> and MSY-SiO<sub>2</sub> samples respectively. Black arrows indicate typical high-intensity points which spectra are presented in c).

The centers of y-axes are close to the centers of studied samples. In both maps, the central and outer regions can be easily distinguished, indicating significant differences in their structures. Fig. 4 c) shows spectra at typical high-intensity points marked by black arrows in Fig. 4 a), b). In both samples, we can observe a signal that can be decomposed into 3 peaks centered at around  $\sim 1470 \text{ cm}^{-1}$ ,  $\sim 1543 \text{ cm}^{-1}$ , and  $\sim 1700 \text{ cm}^{-1}$ . The possible origins of the first of them, reported in the literature, are combinations of C=C stretching and CH wagging Raman modes in trans-polyacetylene diamond grain boundaries introduced during deposition procedure<sup>42</sup> or the presence of amorphous<sup>43</sup> or tetrahedrally-bonded carbon phase<sup>44</sup>. At first glance, the mode at  $\sim 1543 \text{ cm}^{-1}$  could be attributed to the G band in the  $\text{sp}^2$  carbon phase<sup>41,45</sup>. However, as shown later, under 532 nm excitation we can observe the G band in the Raman spectrum of the MSY-SiO<sub>2</sub> sample around  $\sim 1584 \text{ cm}^{-1}$  so at energies around  $40 \text{ cm}^{-1}$  higher. Such a large energy shift cannot be attributed just to a change of the wavelength excitation (as observed for the D band in graphite) so we state that the origin of  $\sim 1543 \text{ cm}^{-1}$  mode observed under 785 nm excitation is different. Based on literature reports we claim that the appearance of a peak in this energy range is related to the presence of oxygen atoms bonded to the edges of graphene/graphite<sup>46,47</sup>. At  $\sim 1700 \text{ cm}^{-1}$  we observe a strong and broad signal, whose origin is not entirely clear to us. Typically, vibrational modes in that range are associated with stretching of the carbonyl group (C=O) in organic compounds like organic acids<sup>48,49</sup>. Such vibrations, attributed to C=O, have been observed in nanodiamonds<sup>50-52</sup>, but usually using infrared-based techniques. Raman

spectroscopy can also reveal the presence of carbonyl groups in diamonds<sup>53</sup>, but the signal typically is not very intense. Therefore, although this interpretation aligns with the proposed origin of the  $\sim 1543\text{ cm}^{-1}$  peak (both suggest the crucial role of oxygen), we do not rule out alternative explanations. Data presented in Fig. 4 a) and b) shows that points, where the Raman signal intensities corresponding to these carbon-related compounds are really strong, are distributed randomly in outer regions of both samples but they form some kind of irregular mesh in central regions. In the case of the sample MSY-SIO2, the same measurements reveal another significant difference between the central and outer regions.

Fig. 5 a) shows the map of a total integrated intensity in the range  $420\text{--}500\text{ cm}^{-1}$  collected from the MSY-SIO2 sample under  $785\text{ nm}$  excitation and Fig. 5 b) presents a spectrum measured at a typical high-intensity point (marked by the black arrow in Fig. 5 a)) where  $\sim 457\text{ cm}^{-1}$  Raman line is observed.

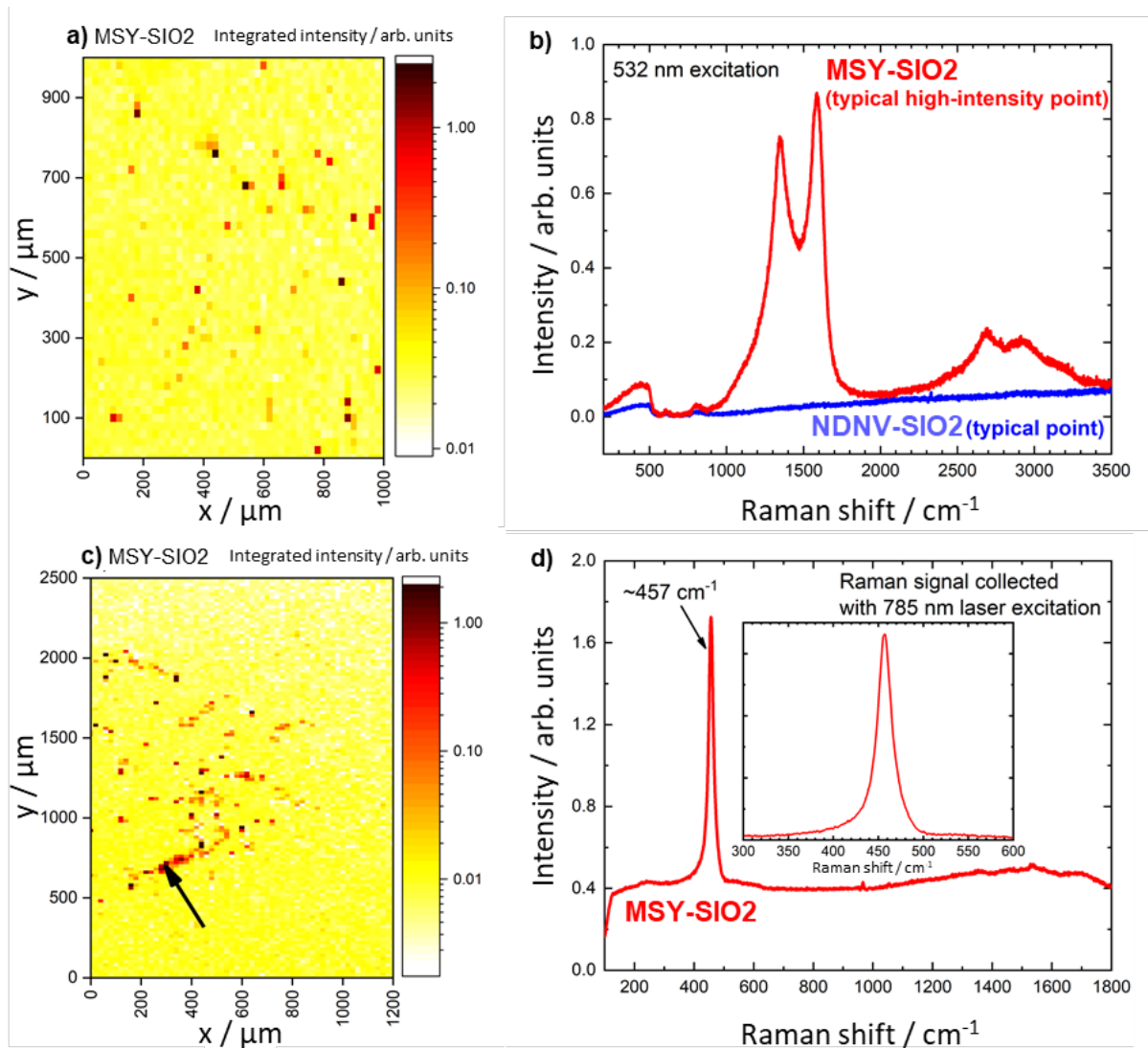


**Fig. 5.** Results of Raman mapping measurement under (a,b) 785 and (c,d) 532 nm laser excitation: a) the map of total integrated intensity in the range 420-500  $\text{cm}^{-1}$  for the MSY-SiO<sub>2</sub> sample, b) the spectrum of a typical high-intensity point indicated by the black arrow in a), c) the map of total integrated intensity in the range 1000-1800  $\text{cm}^{-1}$  for the MSY-SiO<sub>2</sub> sample, d) blue (red) curve – spectrum at a typical (high-intensity) point in the MSY-SiO<sub>2</sub> sample.

The high intensity of this  $\sim 457 \text{ cm}^{-1}$  peak (compared to spectra presented in Fig. 4 c)) and its quite low width (FWHM  $\sim 20 \text{ cm}^{-1}$ ) leads to the conclusion that this mode is related to some well-defined structure that can be easily created in our samples. Therefore, the most obvious explanation would be some Si-related vibration. Indeed, in the literature in that spectral range, some bonds between Si and O atoms are often identified<sup>54–57</sup>. Such interpretation would suggest structural changes of silica on some interfaces between the central and outer regions. This Raman mode is hardly observed in the NDNV-SiO<sub>2</sub> sample. This would suggest that the presence of  $\sim 457 \text{ cm}^{-1}$  mode in the MSY-SiO<sub>2</sub> sample is related to a different process compared to NDNV-SiO<sub>2</sub>. Another explanation would be that the above-mentioned changes in silica are caused by some defects or dopants in MSY particles. Since their structural quality is worse than that of NDNV nanodiamonds (as indicated by the broader  $\sim 1332 \text{ cm}^{-1}$  peak in Fig. S4), one would think about the initiation of some local changes in silica properties. Similar Raman mapping measurements with the same step (20  $\mu\text{m}$ ) have been performed under 532 nm laser excitation but in a smaller area. In such an experiment in the case of MSY-SiO<sub>2</sub> sample, we can observe typical  $\text{sp}^2$ -bonded carbon D-band and G-band around  $\sim 1355 \text{ cm}^{-1}$  and  $\sim 1584 \text{ cm}^{-1}$ <sup>41,45</sup> presented in Fig. 5 d). Also, a 2D overtone ( $\sim 2680 \text{ cm}^{-1}$ ) as well as other combinations of modes at slightly higher energies are presented<sup>58</sup>. The high visibility of these peaks and high G band signal intensity suggest the good quality of the present  $\text{sp}^2$ -hybridized graphene-like material. The map of the integrated total intensity in the range 1000 – 1800  $\text{cm}^{-1}$  for this sample, which is presented in Fig. 5 c), reveals that such structures are randomly distributed over the sample (the left upper corner of the map is close to the center of the sample). However, for the sample NDNV-SiO<sub>2</sub>, in this spectral range we observe only either a small background signal or low-intense luminescence as shown in Fig. 5 d). This suggests that the steps in the decomposition process proceed differently for NDNV and MSY particles.

The fluorescence spectra measured for diamond-doped MSY-SiO<sub>2</sub> and NDNV-SiO<sub>2</sub> preforms, as well as an undoped pure SiO<sub>2</sub> glass used as a reference are presented in Fig. 6 (the sample comes from the same laser vitrification procedure, as the diamond-containing samples).

Samples for fluorescence measurement were prepared in the form of 2 mm long rod sections, polished on both sides. The fluorescence signal was collected from the central part of the polished surface of the rods. All samples show a broad fluorescence band ranging from 580 nm to 700 nm. Although, the origin of this broad fluorescence is difficult to identify, it may be assigned to various types of impurities, admixtures or structural defects resulting from the manufacturing process or remelting technology<sup>59,60</sup>.

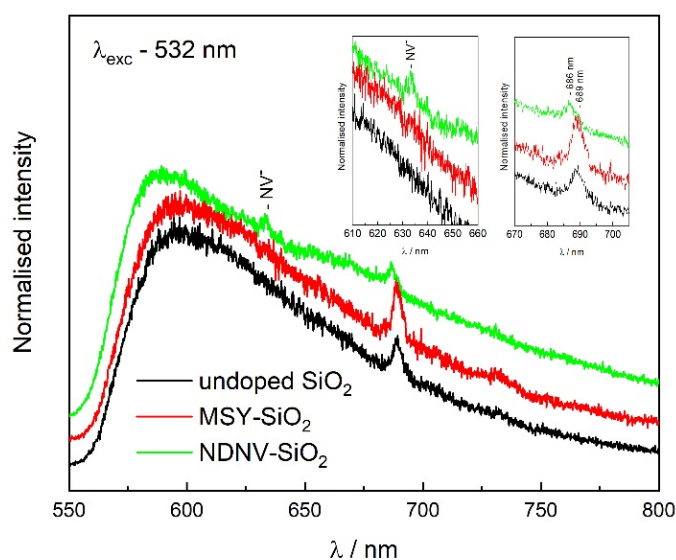


**Fig. 6.** Fluorescence spectra of diamond-doped silica samples (MSY-SiO<sub>2</sub> and NDNV-SiO<sub>2</sub>) and reference undoped, bare silica glass measured under 532 nm laser excitation.

The narrow band with maximum at 689 nm is related to Raman scattering and corresponds to Raman band near 4283 cm<sup>-1</sup>. The intensity of this band increase for doped MSY-SiO<sub>2</sub> sample, and additionally in case of NDNV-SiO<sub>2</sub> sample (inset in Fig. 6) observed band is shifted to 686 nm what corresponds to Raman shift of 4220 cm<sup>-1</sup>. Raman scattering at this range can be assigned to stretching vibration mode of a molecular hydrogen trapped in structure of silica glass, while observed band shift may be related to internal stresses in silica glass<sup>54,61</sup>. For NDNV-SiO<sub>2</sub> sample a very weak band at 637 nm can be seen in the fluorescence spectrum, which can be identified as the resonant optical emission (zero-phonon line, ZPL) from nitrogen-vacancy color center<sup>61</sup>. The narrow ZPL band is assisted by a broad emission band ranging from about 630 up to 750 nm<sup>62</sup>, which in case of NDNV doped fiber is observed as increased fluorescence above 650 nm.

#### 4.1.3 Atomic Composition of vitrified Surfaces by XPS Analysis

The XPS analyses were carried out to investigate the NV-ND chemistry and study changes in ND-silica interface. The registered spectra are presented in Fig. 7 and were deconvoluted using a model discussed below. It should, however, be considered, that the accuracy of quantitative analysis may be limited by the size of the structures being studied. The C 1s spectra for NDNV-SiO<sub>2</sub> sample disclose its complex carbon chemistry, with dominant peak (284.6 eV) characteristic of *sp*<sup>3</sup>-carbon in diamond structure but also carbon contaminants, i.e. adventitious carbon<sup>63</sup>, thus preventing direct diamond phase identification. As a result of ND incorporation in silica, a strong C-Si C 1s signal is visible at 283.9 eV, often reported in the case of diamonds grown on Si substrates<sup>64</sup>. A similar signal may however originate from graphitic *sp*<sup>2</sup>-C phase presence. Finally, one can also observe oxidized carbon species contribution in C 1s (286.0 and 288.1 eV) testifying to the presence of hydroxyl and carboxyl functional groups<sup>65</sup>. The MSY-SiO<sub>2</sub> sample is characterized by significantly higher C-Si share (36% of total [C] content vs 8% for NDNV-SiO<sub>2</sub>) and lower contribution from oxidized C moieties (18% of total [C] vs 36% for NDNV-SiO<sub>2</sub>). The observation is further confirmed by O 1s spectra C-O and C=O signals, which share is 2.5x higher for NDNV-SiO<sub>2</sub> compared with MSY-SiO<sub>2</sub> sample. Detailed analysis was listed in Table 2.

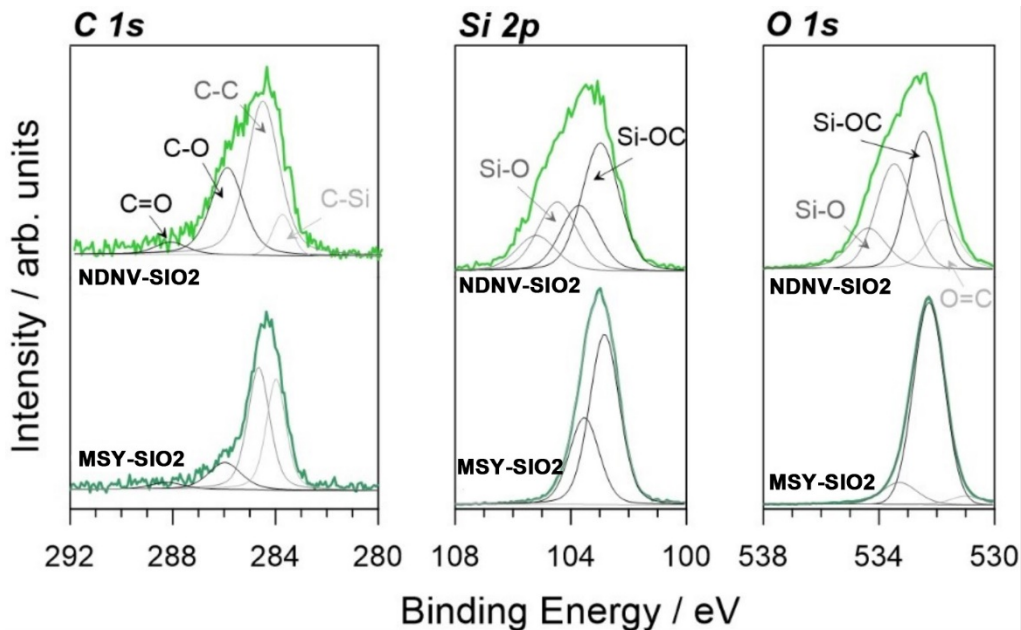


**Fig. 7.** High-resolution XPS spectra recorded for NDNV-SiO<sub>2</sub> and MSY-SiO<sub>2</sub> samples, in C 1s, Si 2p and O 1s binding energy range with proposed deconvolution model.

**Table 2** – Chemical composition (in at.%) of NDNV-SiO<sub>2</sub> and MSY-SiO<sub>2</sub> sample based on discussed deconvolution of high-resolution XPS data.

	<b>C1s</b>				<b>O1s</b>				<b>Si2p</b>	
--	------------	--	--	--	------------	--	--	--	-------------	--

	C-Si	C-C	C-O	C=O	C=O	Si-OC	Si-OH	SiO <sub>2</sub>	Si-OC	SiO <sub>2</sub>
<b>BE</b> [eV]	283.9	284.6	286.0	288.2	531.8	532.4	533.5	534.3	102.8	104.2
<b>NDNV-SiO<sub>2</sub></b>	1.6	11.3	6.4	0.9	7.1	17.6	14.9	6.7	21.4	12.1
<b>MSY-SiO<sub>2</sub></b>	3.6	4.4	1.4	0.4	2.0	45.9	5.8	-	36.4	-

The Si  $2p_{3/2}$  peaking at 103.0 eV and O 1s at 532.4 eV reveal the presence of silicon oxycarbides in both studied samples <sup>66</sup>. Nearly 35 at.% of Si was recorded in both samples based on the XPS analysis. MSY-SiO<sub>2</sub> sample reveal complete SiO<sub>2</sub> to SiO-C transition as a result of sample processing, while NDNV-SiO<sub>2</sub> still contain approx. 36% SiO<sub>2</sub>, identified by Si  $2p_{3/2}$  component at 104.2 eV and O 1s at 534.3 eV <sup>67</sup>. Considering similar share of adventitious carbon for both samples, originating from analogous storage conditions, one may conclude that NDNV-SiO<sub>2</sub> has more unreacted  $sp^3$ -C phase in its structure (C-C signal has 56% of total [C] contribution vs 45% for MSY-SiO<sub>2</sub>). The above analysis suggests that MSY-SiO<sub>2</sub> effectively reacts with SiO<sub>2</sub>, decomposing it to Si-OC at silica-diamond interphase and generating CO<sub>2</sub>, a conclusion confirmed by SEM and simulation results. The CO<sub>2</sub> emission corroborates lower total [C] content in case of MSY-SiO<sub>2</sub> sample. It should be noted that the silica interface possesses catalytic properties towards diamond structure decomposition. The XPS studies reveal that interfacial diamond decomposition to different oxidized carbonaceous entities proceeds at lower temperatures compared with NDNV-SiO<sub>2</sub> that are non-adjacent to silica molecules.

#### 4.1.4 Steps of Thermal Decomposition Studied By TGA/DSC And Mass Spectrometry

The thermal stability and decomposition mechanisms of nanodiamond particles during silica vitrification were investigated using thermogravimetric analysis (TGA) coupled with mass spectrometry (MS) for evolved gas analysis. The thermal decomposition profiles and corresponding MS ion detection data are presented in Figures 8a and b for MSY-SiO<sub>2</sub> and NDNV-SiO<sub>2</sub> composites, respectively. This integrated analytical approach enabled simultaneous monitoring of mass changes and molecular species evolution during the thermal transformation of the nanodiamond-silica systems.

The thermogravimetric measurements revealed minor mass loss profiles for the diamond-silica composites, with total mass losses of 0.002% and 0.009% observed for MSY-SiO<sub>2</sub> and NDNV-SiO<sub>2</sub> samples, respectively. The thermal decomposition exhibited a complex, multi-step character as evidenced by the combined TGA-MS analysis. A notable feature was the evolution of CO<sub>2</sub> molecular ions ( $m/z = 44$ ) detected above 300°C for all samples (Fig. 8), which can be attributed to the release of CO<sub>2</sub> molecules entrapped within the composite matrix during vitrification, corroborating the structural observations from SEM analysis.

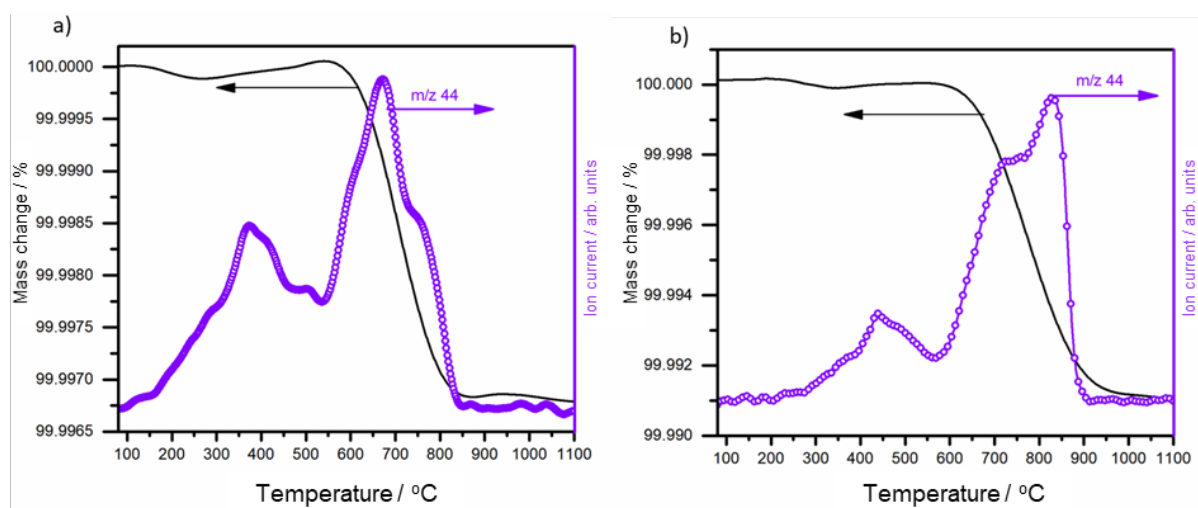


**Fig. 8.** Graphs (a) and (b) display the TGA with the mass spectrometric analysis of the evolved gases for samples MSY-SiO<sub>2</sub> and NDNV-SiO<sub>2</sub>, respectively.

The subsequent decomposition phase, associated with diamond particle thermal degradation, displayed distinct onset temperatures: approximately 550°C for MSY-SiO<sub>2</sub> and 600°C for NDNV-SiO<sub>2</sub><sup>68</sup>. This temperature differential suggests enhanced thermal stability and delayed graphitization of NDNV diamonds compared to their MSY counterparts. These findings can be compared with previous research by Zhang *et al.*<sup>69</sup>, who reported no mass change in pure silica below 1000°C but observed a 0.35% mass decrease in diamond/silica glass composites due to diamond grit oxidation. The significantly lower mass losses in our samples can be attributed to the superior quality of the diamond powders employed in this study compared to the synthetic diamond grit (140/170 US mesh, 90-106 μm) used in<sup>69</sup>.

Particularly, MSY diamond powders demonstrate particular susceptibility to thermal degradation in oxidizing environments<sup>70</sup>, with optimal preservation achieved in hydrogen-containing atmospheres such as forming gas. The onset of weight loss at approximately 500°C for sub-micrometer MSY grade particles, compared to 600-650°C for larger particle sizes<sup>68</sup>, aligns precisely with our observations for MSY (Figure 8a). Intriguingly, NDNV particles

exhibited higher thermal resistance characteristic of larger MSY grains (tens of microns), despite their modest 180 nm size. This enhanced stability can be primarily attributed to acid cleaning procedures implemented to augment NV center emission, resulting in a highly carboxylated surface. Bradac *et al.*<sup>71</sup> provided crucial insights into the relationship between surface chemistry and thermal stability of diamond powders, emphasizing its influence on properties including wetting behavior, surface charge, agglomeration, and chemical reactivity. Their work demonstrated that acid oxidation treatments (HNO<sub>3</sub>, H<sub>2</sub>SO<sub>4</sub>) preferentially generate carboxylic groups, explaining the elevated oxidation resistance of acid-treated NDNV particles compared to untreated MSY powders. Extensive multistage acid purification was shown to increase C-H group content, which exhibits superior oxidation resistance compared to oxygen-containing surface groups. The higher onset temperature (450°C) and maximum weight loss temperature (540°C) may be attributed to reduced metal impurities or modifications in average crystal size, while the broader oxidation temperature range (450-610°C) reflects the complex nature of the thermal decomposition process. The thermal decomposition of MSY and NDNV diamond grains observed in this study, while resulting in minimal mass loss, contrasts significantly with DND behavior<sup>72</sup>, where substantial graphitization and increased porosity occur. However, these minor vitrification-induced mass changes yield similar Raman spectral characteristics in the D, G, and 2D mode regions as illustrated in Fig. 5b.

#### **4.2. Computational Insights using Molecular Dynamics (MD) Simulations**

The thermal stability of the diamond-silica interface was tested uniting the molecular dynamics approach. After the interface models were prepared, as was described in section 3, every structure was subjected to the 120 ps NVT dynamics at 300 K. After this initial phase, the temperature of heat bath was raised to the given value and the simulation was continued through the next 350 ps. The simulation was repeated for 800, 900, 1000, 1150, 1250, 1350, 1450 and 1500 K. The Nosé–Hoover chain thermostat (length of chain 3) was used. Because the Reax FF force field (COHSi<sup>31</sup> parametrisation) was used the bond list was not fixed during simulation time and Verlet list was updated each 4 fs. The special script was written in MATLAB language, which was analysing the LAMMPS trajectory files to estimate the number of free molecules during each step of the simulation. The CO, CO<sub>2</sub>, SiO, SiO<sub>2</sub> and O<sub>2</sub> molecules number was estimated for the whole timespan of the trajectory and it was presented in Fig. 9 for selected simulation results.

Although both stable and unstable interface behavior was observed depending on the temperature used, graphitization did not occur in any of the cases. The scale of the atomic model was insufficient for observation of the graphitization process, in which temperature is significantly dependent on the surface defects and for ideal diamond slabs occur at temperatures close from 2850K for [111] surface to 3680K for [100] surface <sup>73</sup>. The unexpectedly high graphitisation temperature observed in the simulation can be attributed to the scale effect and lack of defects, which accelerates thermal decomposition in real-life materials <sup>74,75</sup>. For the same reasons, it cannot be expected that the thermal decomposition temperature of prepared atomic models of the interface will correlate with the thermogravimetric measurement results exactly. The overestimation of decomposition temperature is predicted. Thus, we decided to focus only on the decomposition process. As was already raised by other authors <sup>76</sup>, the artificially elevated temperature (because of simulation method limitations) of the process does not lead to substantial changes in the products and primarily affects the reaction rate.

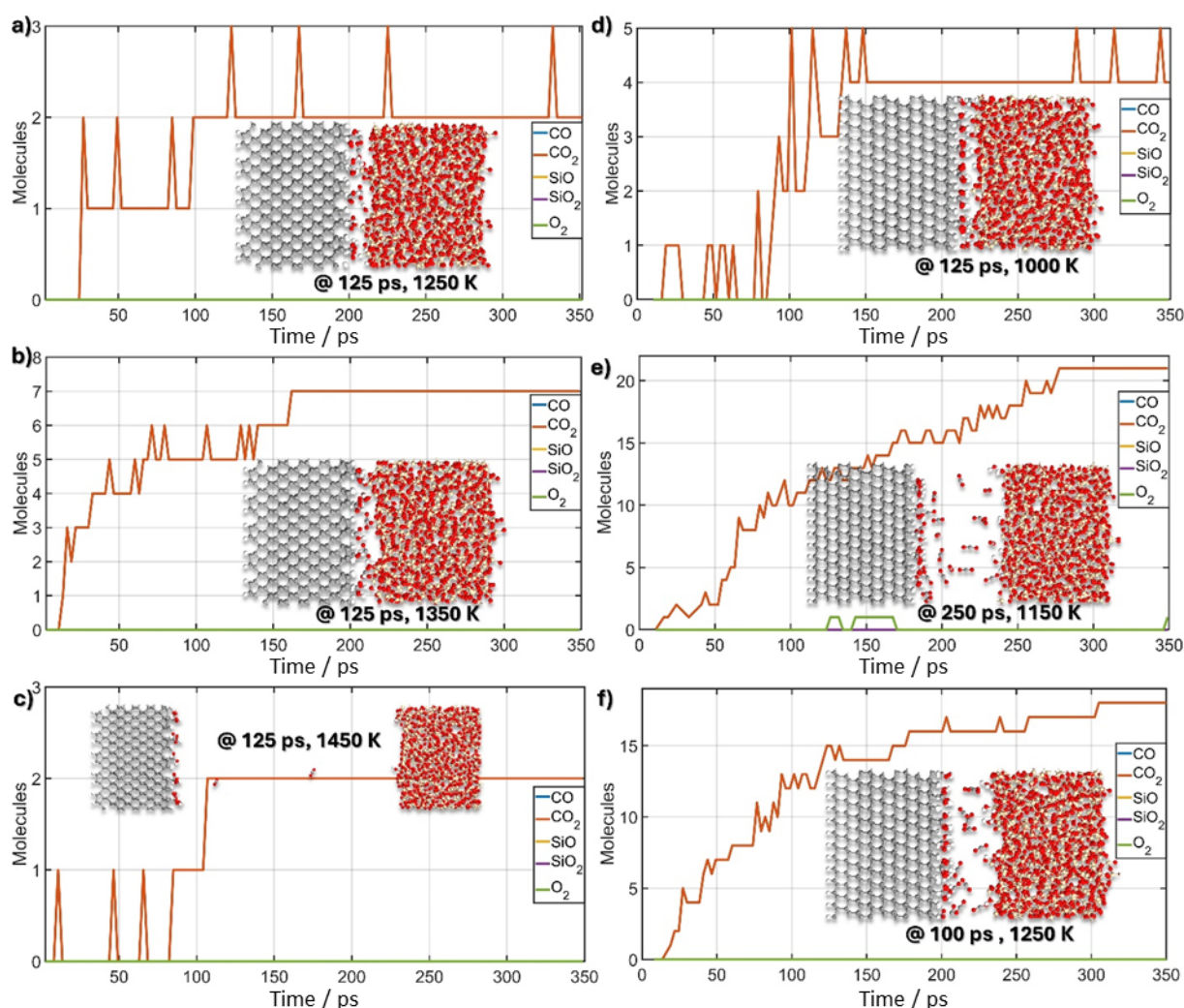


**Fig. 9.** Effect of the different temperature on the diamond silica interface according to the molecular dynamics simulations, for each case the evolution of the number of molecules against

time is shown; the subfigures a, b and c presents interface between the [100] diamond surface and the silica glass for temperatures 1250, 1350 and 1450K, the subfigures d, e and f presents interface between the [111] diamond surface and the silica glass for temperatures 1000, 1150 and 1250K.

Despite both tested diamond surface types, the slab model remains intact, the temperature at which the interface breaks apart is 300K lower for [111] surface than for [100] surface (Fig. 9c and e), which is consistent with lower [111] surface thermal stability<sup>73</sup>. The interface decomposition temperature was estimated to 1150 K for [111] diamond surface and for 1450 K for [100] diamond surface.

Notably, the interface decomposition processes in both cases are similar. At room temperature, the glass slab is held together by O-Si-O bonds which form between carboxyl groups and the silica layer. Until the temperature is more than 100 K lower than the interface decomposition temperature, the minor number of carbon dioxide molecules are formed from carboxyl groups inside the interface: 3 molecules per 6 nm<sup>2</sup> on [100] surface and 5 molecules per 10 nm<sup>2</sup> on the [111] surface (Fig. 9a and 9d). The maximal number of molecules is released when the interface is close to its disintegration temperature: 7 molecules per 6 nm<sup>2</sup> for [100] surface at 1350K and 22 molecules per 6 nm<sup>2</sup> for [111] surface at 1150 K (Fig. 9b and 9e). The future increase in the temperature does not lead to an increase in the rate of CO<sub>2</sub> molecules creation. Once the bonds connecting the silica glass with the diamond are broken and the slabs are separated, the process of the carbon dioxide molecules formation is stopped. Figure 9c presents the low rate of CO<sub>2</sub> emissions despite the significantly higher amount of this gas has been released in the interface at a lower temperature (Fig. 9b). This is also the case for [111] diamond surface, however, the reduction of the rate of release of CO<sub>2</sub> molecules is less significant as can be compared in Figures 9e and 9f.

It could be stated that the release of CO<sub>2</sub> from the carboxylated diamond surface is catalyzed by the presence of the amorphous silica interface. This process leads to the release of the carboxyl groups into the interface, which significantly increases local pressure, which could be observed in Fig. 9b where the surface of silica glass is deformed by the gas pressure. The macroscopic image of this process could be attributed to the formation of the CO<sub>2</sub> bubbles in the glass surface, while the temperature of the interface is increased. Once the temperature becomes high enough the pressure existing in the interface cannot be longer held back by the O-Si-O bonds, which causes rapid delamination of the glass layer.

## Discussion

The experimental observations stem from multiple synergistic phenomena occurring at diamond particle surfaces, influenced by both synthesis methodologies and post-processing treatments. The primary factor driving observed in Raman and XPS transformations is attributed to the integration of diamond surfaces with glass matrices, which necessitate high-temperature fabrication conditions or operation under extreme environments. The crystallographic structure analysis of as-received particles revealed characteristic tetrahedral diamond diffraction patterns dominated by (111) facets<sup>70</sup>. Evans *et al.*<sup>77</sup> conducted systematic investigations of diamond-oxygen reaction kinetics on natural diamond single crystals, examining {111}, {110}, and {100} faces in the temperature range of 650-1350°C. These studies have shown that untreated monocrystalline diamonds with smooth surfaces exhibit enhanced oxidation resistance compared to pre-oxidized specimens with pronounced surface roughness. Furthermore, their findings indicated preferential oxidation of {111} planes below 1000°C, with graphitic layer formation participating in the oxidation mechanism. Our experimental data, however, reveal that the vitrification process conducted under vacuum conditions ( $10^{-6}$  Torr) presents a distinct oxidation pathway compared to literature reports. Raman spectroscopic analysis of our diamond-silica interfaces demonstrates significantly different phase transformation kinetics, with oxygen availability limited predominantly to SiO<sub>2</sub> precursor decomposition. For optical applications, surface chemistry plays a crucial role in determining thermal stability and interface quality. Theije *et al.*<sup>78</sup> demonstrated that water vapor stabilizes {111} planes through -OH termination, with oxidation proceeding via a monoatomic step mechanism leading to shallow etch pit formation. Another study of Theije *et al.*<sup>79</sup> revealed more pronounced oxidative etching on {100} faces of natural type IIa diamonds compared to synthetic type Ib, attributing this to higher dislocation densities. The formation of controlled interfaces is particularly critical for maintaining optical transparency and minimizing scattering at diamond-glass boundaries. Surface morphology and defect structures significantly impact both thermal stability and optical properties. Surface defects, including microcracks, cleavage steps, and step edges, serve as preferential oxidation nucleation sites<sup>80</sup>, which can lead to increased light scattering and reduced optical transmission.

The relationship between particle size and composite properties was extensively investigated by Feng *et al.*<sup>81</sup>, who studied diamond particles ranging from 3-40 μm in borosilicate glass matrices. Their findings revealed that larger particles (30 μm) achieved superior thermal conductivity and mechanical strength through enhanced glass-diamond interfacial bonding.

However, our experimental characterization revealed a critical performance trade-off: enhanced mechanical properties inversely correlated with optical transparency, as measurements demonstrated progressive opacity with increasing diamond particle diameter beyond 100 nm. Our optimization studies determined that diamond particles of 180 nm at concentrations of 10 ppm yielded composites with acceptable optical quality while producing a measurable enhancement in nonlinear refractive index, consistent with <sup>16</sup>. These quantitative relationships between particle parameters and resultant properties provide critical parameters for diamond-silica composite engineering in photonic applications. Surface functionalization significantly influences particle-matrix interactions. Costa *et al.* <sup>82</sup> investigated oxygen-functionalized MSY diamond particles, demonstrating that surface carboxyl groups enhance structural stability. These functional groups may serve dual purposes in optical applications: stabilizing the diamond-glass interface while potentially modifying the local refractive index gradient at particle boundaries.

The thermal stability of diamond-glass interfaces presents significant challenges for composite materials development. Our analysis of recent literature in conjunction with our experimental and computational findings provides critical mechanistic insights into decomposition pathways. Zhang *et al.* <sup>83</sup> demonstrated that Si barrier layers effectively protected diamond particles in borosilicate composites from oxidation up to 1000°C, substantially improving thermal resistance compared to uncoated particles that oxidized at 812°C. However, these protective coatings rendered samples opaque, highlighting the fundamental trade-off between thermal stability and optical transparency in diamond-glass systems. Sun *et al.* <sup>84</sup> provided complementary crystallographic analysis, identifying preferential oxidation initiation at 750 K along {111} planes, while observing non-preferential graphitization around 1100 K under vacuum or inert atmospheres. This temperature differential suggests distinct energetic requirements between oxidative and graphitic transformation pathways. Our theoretical calculations and experimental TGA/mass spectrometry measurements reveal consistent decomposition mechanisms despite expected temperature disparities. The observed simulation overestimation of decomposition temperature remains below 450K, consistent with previously reported phenomena <sup>74,75</sup>. This moderate disparity permits mechanistic interpretation under the established assumption that temperature differences primarily affect reaction rates rather than fundamental processes <sup>76</sup>. Significantly, both TGA experiments and REAXFF calculations demonstrate CO<sub>2</sub> emission during interface heating. Our computational analysis indicates these emissions originate primarily at the interface, generating localized pressure increases that ultimately exceed critical thresholds for structural integrity. The resulting silica delamination

produces characteristic bubble-like surface defects, which our SEM imaging confirms, providing direct experimental validation of the theoretically predicted mechanism.

The morphological characteristics of fluorescent diamond particles, as reported for various commercially available materials<sup>85</sup>, indicate distinct aspect ratios and preferential cleavage planes as revealed also in our studies. These particles typically exhibit disk- or rod-like shapes with width-to-height ratios between 2:1 and 3:1, while single-particle AFM measurements reveal aspect ratios exceeding 4:1. The preferential cleavage along specific crystallographic planes - whether {111} due to minimal bond breaking requirements or {110} based on maximum stress considerations<sup>86</sup> - has significant implications for optical properties, particularly regarding polarization-dependent scattering and absorption. Reported findings collectively emphasize the complex interplay between particle size, surface chemistry, processing conditions, and resulting optical properties in diamond-glass composites. While larger particles may offer superior thermal and mechanical properties, their use compromises optical transparency. Conversely, smaller particles maintain better optical properties but present challenges in terms of thermal stability and interface control. Future developments in this field will require careful optimization of these competing factors to achieve both thermal stability and optical functionality.

An overview of previously reported diamond incorporation strategies into silica glass matrices, summarized in Table 3, reveals significant methodological diversity in diamond-silica interface engineering, with varying degrees of optimization achieved across optical performance metrics. The observed heterogeneity in fabrication approaches reflects both the complexity of interface control and the diverse requirements for specific photonic applications. While chemical functionalization approaches (ND-COOH/silyl-ether formation) demonstrate controlled interface formation, the inverse correlation between SiO<sub>2</sub> encapsulation and ZPL intensity suggests suboptimal photonic coupling. Sol-gel methodologies achieve uniform dispersion but require complex thermal protocols, potentially impacting NV center stability. Notably, the mechanical van der Waals integration exhibits superior photon collection efficiency (37%), though scalability remains uncertain. The latest bulk integration approach, while enabling direct preform fabrication, yields comparatively weak ZPL luminescence, indicating potential interface quality challenges despite achieving modified nonlinear optical properties.

**Table 3** - Fabrication approaches and optical performance of nanodiamond-incorporation into silica glass samples.

Name	Fabrication strategy	Diamond particles types	Optical performance	Reference
Tellurite glass step index fibers	Melting of tellurite glass from raw materials at 690°C, followed by introduction of nanodiamonds into the melt at decreased temperature of 610°C, then casting into billets, extruding and drawing into optical fibers	NV-rich nanodiamonds with 40-50 nm average size	NV-diamond's ZPL at 637 nm, ODMR measurements with 10 $\mu\text{T}/\text{Hz}^{1/2}$ sensitivity, 9-14 dB/m fiber attenuation	<sup>87,88</sup>
F2 glass fibers with nanodiamond ring surrounding the optical fiber core area	Dip-coating of an F2 rod and redrawing in an F2 tube into an optical fiber	HPHT NV-rich diamond particles with ca. 1 $\mu\text{m}$ average size	Bright ZPL luminescence and ODMR signals, between 350nT <sup>1/2</sup> and 3 $\mu\text{T}/\text{Hz}^{1/2}$ magnetic field sensitivity depending on the collection scheme, 50 cm of practical fiber length, 4 dB/m attenuation	<sup>89</sup>
F2 glass nanostructured ND-doped multimode fibers (ND distributed in the volume of the optical fiber core)	Dip-coating, restacking multiple ND-coated canes and redrawing into final optical fibers	HPHT NV-rich sub-micron diamonds with ca. 750 nm average size	bright ZPL luminescence and ODMR signals, 5 $\mu\text{T}/\text{Hz}^{1/2}$ magnetic field sensitivity in full transmission mode, 15 cm of practical fiber length, 20 dB/m attenuation	<sup>90</sup>
Nanoparticles in the form of nanodiamond cores in SiO <sub>2</sub> encapsulating shells	Rehydroxylation HPHT nanodiamonds (ND-COOH) to form silyl-ether bonds on the diamond surface from tetraethyl orthosilicate precursors, followed by amorphous SiO <sub>2</sub> growth on ND surface in presence of ethanol, ammonium hydroxide and water	HPHT NV-rich ND, 5-30 nm size	Detectable ZPL of NV(-) color centers, 637 nm, intensity diminishing with thickness of the SiO <sub>2</sub> encapsulation	<sup>91</sup>
2 $\mu\text{m}$ -thick films of homogeneously dispersed ND in an amorphous SiO <sub>2</sub> , spin-cast on cover glass slips	Films prepared by sol-gel; the sol obtained from tetraethyl orthosilicate precursor, ND dispersed in the sol using ultrasonic centrifugation, followed by annealing at 800°C and then at 550°C to remove graphite from surface, final annealing at	NV-rich ND with 78 $\pm$ 2 nm mean fraction	Temperature-dependent ZPL luminescence of NV(-) centers, incl. redshift by ca. 2 nm.	<sup>92</sup>

	200°C applied after spin-coating the films of coverslips			
Diamond thin films, each with the following parameters: 200 nm thickness × 12 μm length, placed on a SiO <sub>2</sub> fiber taper and fixed by van der Waals forces	Lithography-based fabrication of diamond waveguides followed by positioning on silica fiber tapers using a micro-manipulator	200 nm thick single crystal diamond films grown using CVD, each containing a single NV center	37% collection efficiency of NV fluorescence (ZPL at 637 nm) into a the fundamental fiber mode. The NV centers exhibit a pronounced zero-phonon line at 637 nm. Single photon detection rate exceeding 600,000 counts/s	<sup>93</sup>
Silica glass rods (optical fiber preforms) with 5 mm outer diameter, nanodiamonds and carbon material in the central area of the preform	Mixing of ready silica sol-gel granulates and nanodiamonds inside a silica glass tube, followed by vitrification using a high power laser beam “blade”	NV-rich nanodiamonds with 180 nm average size	Optical quality material with weak ZPL luminescence observable from bright luminescent spots within the bulk of sample, 20% decrease of nonlinear refractive index (at 1030 nm) compared to pure silica glass	This work and <sup>16</sup>

Cutting-edge research is leveraging these properties for the development of next-generation devices. For example, ND doped with nitrogen-vacancy centers are being explored for their potential in quantum computing and high-resolution sensing due to their stable photoluminescence characteristics <sup>91</sup>. Furthermore, there is ongoing research into the use of microdiamond particles in thermal management solutions for electronics and photonics. While the potential applications for ND and microdiamonds are vast, the challenge lies in the synthesis, functionalization, and integration of these materials into existing systems. The current state of the art involves tailoring the surface chemistry of these diamond particles to optimize their dispersion, stability, and interface with other materials for specific applications <sup>94</sup>. In a notable finding, Tsukahara et al. <sup>95</sup> disclosed that the aerobic oxidation of nanodiamond at 550°C facilitates an enhancement in the transverse spin-coherence time (T<sub>2</sub>) of nitrogen-vacancy (NV) centers. This improvement is pivotal for augmenting the sensitivity of NV centers in quantum sensing applications.

## Conclusions

These results unlock new understanding of the thermal decomposition mechanisms at silica-diamond interfaces during laser vitrification. We came across significant differences in thermal

stability and decomposition pathways between NDNV-SiO<sub>2</sub> and MSY-SiO<sub>2</sub> composites. The NDNV-SiO<sub>2</sub> composite exhibits superior homogeneity with minimal defect formation, attributed to the controlled nitrogen implantation and acid treatment. This surface modification proves instrumental in elevating the thermal decomposition. In contrast, MSY-SiO<sub>2</sub> samples display defect aggregates reaching 10 μm in diameter and 20-30 μm spacing, stemming from accelerated decomposition of diamonds with undefined surface termination.

Analysis of oxygen-functionalized MSY diamond particles demonstrated that surface carboxyl groups significantly enhance structural stability. These functional groups serve a dual role: providing thermodynamic stabilization and offering kinetic protection by forming a protective surface layer, which are both critical during thermal processing. Raman scattering mapping revealed complex structural transitions, particularly at the interfaces. The spectra indicated the formation of various carbon-related compounds, suggesting the presence of C=C stretching, oxygen-bonded graphene edges, and carbonyl groups. A distinct 457 cm<sup>-1</sup> Raman line observed in MSY-SiO<sub>2</sub> samples at interface boundaries, indicated significant structural modifications of silica. The preservation of NV centers in NDNV-SiO<sub>2</sub> samples is confirmed by the characteristic 637 nm zero-phonon line emission. XPS analysis demonstrated markedly different interfacial chemistry, with MSY-SiO<sub>2</sub> showing significantly higher C-Si bonding (36%) compared to NDNV-SiO<sub>2</sub> (8%). The complete transformation of SiO<sub>2</sub> to SiO-C in MSY-SiO<sub>2</sub> samples contrasts with NDNV-SiO<sub>2</sub>, which maintains approximately 36% unreacted SiO<sub>2</sub>, indicating distinct reaction pathways.

Thermal analysis through TGA-MS revealed a multi-step decomposition process, with initial CO<sub>2</sub> release above 300°C followed by diamond degradation at higher temperatures. The NDNV-SiO<sub>2</sub> system demonstrates enhanced thermal stability with decomposition onset at 600°C, compared to 550°C for MSY-SiO<sub>2</sub>. This temperature differential proves crucial for maintaining structural integrity during the vitrification process.

The molecular dynamics simulations revealed distinct decomposition temperatures for different crystal orientations: 1150 K for [111] and 1450 K for [100] diamond surfaces. This 300 K difference aligns with the fundamental thermal stability characteristics of these crystal faces. A particularly significant finding from the MD studies was the quantification of CO<sub>2</sub> evolution at different temperatures and crystal orientations. The [111] surface exhibited higher reactivity, producing 22 molecules per 6 nm<sup>2</sup> at 1150 K, compared to 7 molecules per 6 nm<sup>2</sup> for the [100] surface at 1350 K. This molecular-level understanding reveals highlights how interfacial pressure buildup from CO<sub>2</sub> formation ultimately leads to delamination when O-Si-O bonds can no longer contain the increasing pressure. The integration of experimental and computational

results establishes a comprehensive model of thermal decomposition at silica-diamond interfaces. The catalytic role of the amorphous silica interface in CO<sub>2</sub> release from carboxylated diamond surfaces represents a crucial mechanism controlling interface stability. These findings provide essential guidance for optimizing processing parameters in the development of diamond-silica composites for quantum sensing and optical fiber applications.

This research significantly advances our understanding of diamond-silica interface chemistry and provides a foundation for developing more stable composite materials through careful control of surface termination and processing conditions. The combination of advanced characterization techniques with molecular dynamics simulations offers a powerful approach for future materials design in quantum technology applications.

### **Declaration of Competing Interest**

The authors declare that they have no known competing financial interests or personal relationships that could have appeared to influence the work reported in this paper.

### **Data availability**

All data analyzed during the study are included in this article and will be made upon reasonable request.

### **Acknowledgments**

The research was carried out within the TEAM NET programme of the Foundation for Polish Science co-financed by the European Union under the European Regional Development Fund, project POIR.04.04.00-00-1644/18. We gratefully acknowledge Polish high-performance computing infrastructure PLGrid (HPC Centers: ACK Cyfronet AGH, CI TASK) for providing computer facilities and support within computational grant no. PLG/2023/016164

### **Declaration of generative AI and AI-assisted technologies in the writing process**

During the preparation of this manuscript, the authors utilized Claude AI for grammar correction. The authors reviewed and edited all AI-suggested changes and take full responsibility for the final content of the publication.

## References

- 1 V. Mochalin, O. Shenderova, D. Ho and Y. Gogotsi, in *Nano-Enabled Medical Applications*, Jenny Stanford Publishing, 2020.
- 2 J.-C. Arnault, *Nanodiamonds: Advanced Material Analysis, Properties and Applications*, William Andrew, 2017.
- 3 L. Arnoldi, M. Spies, J. Houard, I. Blum, A. Etienne, R. Ismagilov, A. Obraztsov and A. Vella, *Applied Physics Letters*, 2018, **112**, 143104.
- 4 S. V. Kidalov, F. M. Shakhov and A. Ya. Vul, *Diamond and Related Materials*, 2008, **17**, 844–847.
- 5 C. Bradac and S. Osswald, *Carbon*, 2018, **132**, 616–622.
- 6 V. P. Efremov and E. I. Zakatilova, *J. Phys.: Conf. Ser.*, 2016, **774**, 012014.
- 7 E. Ekimov, A. A. Shiryaev, Y. Grigoriev, A. Averin, E. Shagieva, S. Stehlik and M. Kondrin, *Nanomaterials*, 2022, **12**, 351.
- 8 M. D. Torelli, N. A. Nunn, Z. R. Jones, T. Vedelaar, S. K. Padamati, R. Schirhagl, R. J. Hamers, A. I. Shames, E. O. Danilov, A. Zaitsev and O. A. Shenderova, *Front. Phys.*, DOI:10.3389/fphy.2020.00205.
- 9 I. A. Dobrinets, V. G. Vins and A. M. Zaitsev, *HPHT-Treated Diamonds: Diamonds Forever*, Springer, Berlin, 2013th edition., 2013.
- 10 Z. Qiao, J. Li, N. Zhao, C. Shi and P. Nash, *Scripta Materialia*, 2006, **54**, 225–229.
- 11 Yu. V. Butenko, V. L. Kuznetsov, E. A. Paukshtis, A. I. Stadnichenko, I. N. Mazov, S. I. Moseenkov, A. I. Boronin and S. V. Kosheev, *Fullerenes, Nanotubes and Carbon Nanostructures*, 2006, **14**, 557–564.
- 12 J. Qian, C. Pantea, J. Huang, T. W. Zerda and Y. Zhao, *Carbon*, 2004, **42**, 2691–2697.
- 13 Yu. V. Butenko, V. L. Kuznetsov, A. L. Chuvilin, V. N. Kolomiichuk, S. V. Stankus, R. A. Khairulin and B. Segall, *Journal of Applied Physics*, 2000, **88**, 4380–4388.
- 14 S. V. Kidalov, F. M. Shakhov and A. Ya. Vul, *Diamond and Related Materials*, 2008, **17**, 844–847.
- 15 A. Filipkowski, M. Mrózek, G. Stępniewski, M. Ficek, D. Pysz, W. Gawlik, R. Buczyński, A. Wojciechowski and M. Klimczak, *Applied Physics Letters*, 2024, **124**, 231104.
- 16 G. Stępniewski, P. Hänzi, A. Filipkowski, M. Janik, M. Mrózek, Y. Stepanenko, R. Bogdanowicz, V. Romano, A. Heidt, R. Buczyński and M. Klimczak, *Carbon*, 2023, **215**, 118465.
- 17 N. Khosravian, M. K. Samani, G. C. Loh, G. C. K. Chen, D. Baillargeat and B. K. Tay, *Journal of Applied Physics*, 2013, **113**, 024907.
- 18 X. Wang, X. Song, H. Wang, Y. Qiao, K. Larsson and F. Sun, *ACS Appl. Mater. Interfaces*, 2020, **12**, 42302–42313.
- 19 A. Peguiron, G. Moras, M. Walter, H. Uetsuka, L. Pastewka and M. Moseler, *Carbon*, 2016, **98**, 474–483.
- 20 P. J. Sandoval, K. Lopez, A. Arreola, A. Len, N. Basravi, P. Yamaguchi, R. Kawamura, C. X. Stokes, C. Melendrez, D. Simpson, S.-J. Lee, C. J. Titus, V. Altoe, S. Sainio, D. Nordlund, K. Irwin and A. Wolcott, *ACS Nanosci. Au*, 2023, **3**, 462–474.
- 21 P. E. Pehrsson, T. W. Mercer and J. A. Chaney, *Surface Science*, 2002, **497**, 13–28.
- 22 V. Ya. Shevchenko, S. N. Perevislov and V. L. Ugolkov, *Glass Phys Chem*, 2021, **47**, 197–208.
- 23 J. Liang, Y. Zhou, S. Masuya, F. Gucmann, M. Singh, J. Pomeroy, S. Kim, M. Kuball, M. Kasu and N. Shigekawa, *Diamond and Related Materials*, 2019, **93**, 187–192.
- 24 X. Wang, X. Song, H. Wang, Y. Qiao, K. Larsson and F. Sun, *ACS Appl. Mater. Interfaces*, 2020, **12**, 42302–42313.
- 25 E. R. Wilson, L. M. Parker, A. Orth, N. Nunn, M. Torelli, O. Shenderova, B. C. Gibson and P. Reineck, *Nanotechnology*, 2019, **30**, 385704.
- 26 P. Hänzi, D. Pysz, M. Mrózek, R. Bogdanowicz, R. Buczynski, M. Klimczak, T. Feuerer, V. Romano and A. Heidt, *Optical Materials Express*, DOI:10.1364/OME.546496.
- 27 T. P. Senftle, S. Hong, M. M. Islam, S. B. Kylasa, Y. Zheng, Y. K. Shin, C. Junkermeier, R. Engel-Herbert, M. J. Janik, H. M. Aktulga, T. Verstraelen, A. Grama and A. C. T. van Duin, *npj Comput Mater*, 2016, **2**, 1–14.

- 28 N. Nayir, A. C. T. van Duin and S. Erkoç, *J. Phys. Chem. A*, 2019, **123**, 4303–4313.
- 29 P. K. Weiner and P. A. Kollman, *Journal of Computational Chemistry*, 1981, **2**, 287–303.
- 30 B. R. Brooks, C. L. Brooks III, A. D. Mackerell Jr., L. Nilsson, R. J. Petrella, B. Roux, Y. Won, G. Archontis, C. Bartels, S. Boresch, A. Caflisch, L. Caves, Q. Cui, A. R. Dinner, M. Feig, S. Fischer, J. Gao, M. Hodoscek, W. Im, K. Kuczera, T. Lazaridis, J. Ma, V. Ovchinnikov, E. Paci, R. W. Pastor, C. B. Post, J. Z. Pu, M. Schaefer, B. Tidor, R. M. Venable, H. L. Woodcock, X. Wu, W. Yang, D. M. York and M. Karplus, *Journal of Computational Chemistry*, 2009, **30**, 1545–1614.
- 31 D. A. Newsome, D. Sengupta, H. Foroutan, M. F. Russo and A. C. T. van Duin, *J. Phys. Chem. C*, 2012, **116**, 16111–16121.
- 32 S. Yuan, X. Guo, P. Li, Q. Mao, M. Lu, Z. Jin, R. Kang and D. Guo, *Applied Surface Science*, 2021, **540**, 148321.
- 33 S. Smidstrup, T. Markussen, P. Vancraeyveld, J. Wellendorff, J. Schneider, T. Gunst, B. Verstichel, D. Stradi, P. A. Khomyakov, U. G. Vej-Hansen, M.-E. Lee, S. T. Chill, F. Rasmussen, G. Penazzi, F. Corsetti, A. Ojanperä, K. Jensen, M. L. N. Palsgaard, U. Martinez, A. Blom, M. Brandbyge and K. Stokbro, *J. Phys.: Condens. Matter*, 2019, **32**, 015901.
- 34 Y. Tian and K. Larsson, *J. Material Sci Eng*, DOI:10.4172/2169-0022.1000506.
- 35 H. Gomez, M. N. Groves and M. R. Neupane, *Carbon Trends*, 2021, **3**, 100033.
- 36 A. Pedone, G. Malavasi, M. C. Menziani, A. N. Cormack and U. Segre, *J. Phys. Chem. B*, 2006, **110**, 11780–11795.
- 37 A. P. Thompson, H. M. Aktulga, R. Berger, D. S. Bolintineanu, W. M. Brown, P. S. Crozier, P. J. in 't Veld, A. Kohlmeyer, S. G. Moore, T. D. Nguyen, R. Shan, M. J. Stevens, J. Tranchida, C. Trott and S. J. Plimpton, *Computer Physics Communications*, 2022, **271**, 108171.
- 38 O. A. Shenderova, A. I. Shames, N. A. Nunn, M. D. Torelli, I. Vlasov and A. Zaitsev, *Journal of Vacuum Science & Technology B*, 2019, **37**, 030802.
- 39 J. Qian, C. Pantea, J. Huang, T. W. Zerda and Y. Zhao, *Carbon*, 2004, **42**, 2691–2697.
- 40 S. Stehlik, M. Varga, M. Ledinsky, V. Jirasek, A. Artemenko, H. Kozak, L. Ondic, V. Skakalova, G. Argentero, T. Pennycook, J. C. Meyer, A. Fejfar, A. Kromka and B. Rezek, *J. Phys. Chem. C*, 2015, **119**, 27708–27720.
- 41 D. S. Knight and W. B. White, *Journal of Materials Research*, 1989, **4**, 385–393.
- 42 A. C. Ferrari and J. Robertson, *Phys. Rev. B*, 2001, **63**, 121405.
- 43 R. E. Shroder, R. J. Nemanich and J. T. Glass, *Phys. Rev. B*, 1990, **41**, 3738–3745.
- 44 B. Marcus, L. Fayette, M. Mermoux, L. Abello and G. Lucazeau, *Journal of Applied Physics*, 1994, **76**, 3463–3470.
- 45 A. C. Ferrari and J. Robertson, *Phys. Rev. B*, 2000, **61**, 14095–14107.
- 46 S. Claramunt, A. Varea, D. López-Díaz, M. M. Velázquez, A. Cornet and A. Cirera, *J. Phys. Chem. C*, 2015, **119**, 10123–10129.
- 47 T. Milenov, D. Trifonov, D. A. Kalchevski, S. Kolev, I. Avramova, S. Russev, K. Genkov, G. Avdeev, D. Dimov, D. M. Karaivanova and E. Valcheva, *Materials*, 2023, **16**, 7190.
- 48 G. Socrates, *Infrared and Raman Characteristic Group Frequencies: Tables and Charts*, Wiley, Chichester, 3rd edition., 2004.
- 49 J. Dong, Y. Ozaki and K. Nakashima, *Macromolecules*, 1997, **30**, 1111–1117.
- 50 P. Aprà, N. H. Amine, A. Britel, S. Sturari, V. Varzi, M. Ziino, L. Mino, P. Olivero and F. Picollo, *Advanced Functional Materials*, 2024, **34**, 2404831.
- 51 S. Sturari, V. Varzi, P. Aprà, A. Britel, N.-H. Amine, G. Andriani, E. Corte, G. Tomagra, L. Mino, P. Olivero and F. Picollo, *Surfaces and Interfaces*, 2023, **38**, 102831.
- 52 T. Petit and L. Puskar, *Diamond and Related Materials*, 2018, **89**, 52–66.
- 53 M. L. Frezzotti, *Nat Commun*, 2019, **10**, 4952.
- 54 P. McMillan, B. Piriou and R. Couty, *The Journal of Chemical Physics*, 1984, **81**, 4234–4236.
- 55 P. Borowicz, A. Taube, W. Rzodkiewicz, M. Latek and S. Gierałtowska, *The Scientific World Journal*, 2013, **2013**, 208081.
- 56 T. P. Nguyen and S. Lefrant, *Solid State Communications*, 1986, **57**, 235–236.
- 57 P. McMillan, *American Mineralogist*, 1984, **69**, 622–644.

- 58 M. Zeiger, N. Jäckel, M. Aslan, D. Weingarth and V. Presser, *Carbon*, 2015, **84**, 584–598.
- 59 R. Jedamzik, F. Elsmann, A. Engel, U. Petzold and J. Pleitz, in *Current Developments in Lens Design and Optical Engineering XVIII*, SPIE, 2017, vol. 10375, pp. 49–59.
- 60 M. A. Fikiert, D. Tuschel, V. V. Ermolenkov and I. K. Lednev, *Appl Spectrosc*, 2020, **74**, 187–192.
- 61 K. V. Bogdanov, M. V. Zhukovskaya, V. Yu. Osipov, E. V. Ushakova, M. A. Baranov, K. Takai, A. Rampersaud and A. V. Baranov, *APL Materials*, 2018, **6**, 086104.
- 62 K. Beha, H. Fedder, M. Wolfer, M. C. Becker, P. Siyushev, M. Jamali, A. Batalov, C. Hinz, J. Hees, L. Kirste, H. Obloh, E. Gheeraert, B. Naydenov, I. Jakobi, F. Dolde, S. Pezzagna, D. Twittchen, M. Markham, D. Dregely, H. Giessen, J. Meijer, F. Jelezko, C. E. Nebel, R. Bratschitsch, A. Leitenstorfer and J. Wrachtrup, *Beilstein J. Nanotechnol.*, 2012, **3**, 895–908.
- 63 L. H. Grey, H.-Y. Nie and M. C. Biesinger, *Applied Surface Science*, 2024, **653**, 159319.
- 64 B. Humbert, N. Hellala, J. J. Ehrhardt, S. Barrat and E. Bauer-grosse, *Applied Surface Science*, 2008, **254**, 6400–6409.
- 65 R. Bogdanowicz and J. Ryl, *Current Opinion in Electrochemistry*, 2022, **31**, 100876.
- 66 A. Kaur, P. Chahal and T. Hogan, *IEEE Electron Device Letters*, 2016, **37**, 142–145.
- 67 M. Çopuroğlu, H. Sezen, R. L. Opila and S. Suzer, *ACS Appl. Mater. Interfaces*, 2013, **5**, 5875–5881.
- 68 O. Beffort, S. Vaucher and F. A. Khalid, *Diamond and Related Materials*, 2004, **13**, 1834–1843.
- 69 Y. Zhang, Q. Hua, J. M. Zhang, Y. Zhao, H. Yin, Z. Dai, L. Zheng and J. Tang, *Nanocomposites*, 2018, **4**, 58–67.
- 70 O. Beffort, S. Vaucher and F. A. Khalid, *Diamond and Related Materials*, 2004, **13**, 1834–1843.
- 71 C. Bradac and S. Osswald, *Carbon*, 2018, **132**, 616–622.
- 72 M. Zeiger, N. Jäckel, M. Aslan, D. Weingarth and V. Presser, *Carbon*, 2015, **84**, 584–598.
- 73 J. Yu, G. Liu, A. V. Sumant, V. Goyal and A. A. Balandin, *Nano Lett.*, 2012, **12**, 1603–1608.
- 74 K. Shirai, H. Momida, K. Sato and S. Hyun, *J. Phys.: Condens. Matter*, 2025, **37**, 135901.
- 75 T. Lukinov, A. Rosengren and A. B. Belonoshko, *Computational Materials Science*, 2013, **79**, 95–98.
- 76 X. Li, M. Zheng, C. Ren and L. Guo, *Energy Fuels*, 2021, **35**, 11707–11739.
- 77 J. E. Field, *The Properties of Diamond*, Academic Press, London ; New York, First Edition., 1979.
- 78 F. K. de Theije, E. van Veenendaal, W. J. P. van Enckevort and E. Vlieg, *Surface Science*, 2001, **492**, 91–105.
- 79 F. K. de Theije, O. Roy, N. J. van der Laag and W. J. P. van Enckevort, *Diamond and Related Materials*, 2000, **9**, 929–934.
- 80 P. John, N. Polwart, C. E. Troupe and J. I. B. Wilson, *Diamond and Related Materials*, 2002, **11**, 861–866.
- 81 D. Feng, Z. Li, Y. Zhu and H. Ji, *Materials Science and Engineering: B*, 2018, **227**, 122–128.
- 82 G. C. C. Costa, O. Shenderova, V. Mochalin, Y. Gogotsi and A. Navrotsky, *Carbon*, 2014, **80**, 544–550.
- 83 X. H. Zhang, Y. H. Wang, J. B. Zang, J. Lu, J. H. Zhang, E. B. Ge and X. Z. Cheng, *Surface and Coatings Technology*, 2010, **204**, 2846–2850.
- 84 C. Q. Sun, H. Xie, W. Zhang, H. Ye and P. Hing, *J. Phys. D: Appl. Phys.*, 2000, **33**, 2196.
- 85 S. Eldemrashed, G. Thalassinou, A. Alzahrani, Q. Sun, E. Walsh, E. Grant, H. Abe, T. L. Greaves, T. Ohshima, P. Cigler, P. Matějčík, D. A. Simpson, A. D. Greentree, G. Bryant, B. C. Gibson and P. Reineck, *Carbon*, 2023, **206**, 268–276.
- 86 O. A. Shenderova and G. E. McGuire, *Biointerphases*, 2015, **10**, 030802.
- 87 Y. Ruan, H. Ji, B. C. Johnson, T. Ohshima, A. D. Greentree, B. C. Gibson, T. M. Monro and H. Ebdorff-Heidepriem, *Opt. Mater. Express*, 2015, **5**, 73–87.
- 88 Y. Ruan, D. A. Simpson, J. Jeske, H. Ebdorff-Heidepriem, D. W. M. Lau, H. Ji, B. C. Johnson, T. Ohshima, S. Afshar V., L. Hollenberg, A. D. Greentree, T. M. Monro and B. C. Gibson, *Sci Rep*, 2018, **8**, 1268.
- 89 D. Bai, M. H. Huynh, D. A. Simpson, P. Reineck, S. A. Vahid, A. D. Greentree, S. Foster, H. Ebdorff-Heidepriem and B. C. Gibson, *APL Materials*, 2020, **8**, 081102.

- 90 A. Filipkowski, M. Mrózek, G. Stępniewski, J. Kierdaszuk, A. Drabińska, T. Karpate, M. Głowacki, M. Ficek, W. Gawlik, R. Buczyński, A. Wojciechowski, R. Bogdanowicz and M. Klimczak, *Carbon*, 2022, **196**, 10–19.
- 91 P. J. Sandoval, K. Lopez, A. Arreola, A. Len, N. Basravi, P. Yamaguchi, R. Kawamura, C. X. Stokes, C. Melendrez, D. Simpson, S.-J. Lee, C. J. Titus, V. Altoe, S. Sainio, D. Nordlund, K. Irwin and A. Wolcott, *ACS Nanosci. Au*, 2023, **3**, 462–474.
- 92 X. Jing, Y. Xu, H. Gan, P. Hu, C. Li, J. Qian, J. Zhang, Y. Tian and S. Xu, *Carbon*, 2021, **184**, 303–311.
- 93 R. N. Patel, T. Schröder, N. Wan, L. Li, S. L. Mouradian, E. H. Chen and D. R. Englund, *Light Sci Appl*, 2016, **5**, e16032–e16032.
- 94 E. Mayerhoefer and A. Krueger, *Acc. Chem. Res.*, 2022, **55**, 3594–3604.
- 95 R. Tsukahara, M. Fujiwara, Y. Sera, Y. Nishimura, Y. Sugai, C. Jentgens, Y. Teki, H. Hashimoto and S. Shikata, *ACS Appl. Nano Mater.*, 2019, **2**, 3701–3710.